

A Nitsche-type formulation and comparison of the most common domain decomposition methods in isogeometric analysis

Andreas Apostolatos^{*,†}, Robert Schmidt, Roland Wüchner and Kai-Uwe Bletzinger

Lehrstuhl für Statik, Technische Universität München, Arcisstrasse 21, D-80333 Munich, Germany

SUMMARY

This paper provides a detailed elaboration and assessment of the most common domain decomposition methods for their application in isogeometric analysis. The methods comprise a penalty approach, Lagrange multiplier methods, and a Nitsche-type method. For the Nitsche method, a new stabilized formulation is developed in the context of isogeometric analysis to guarantee coercivity. All these methods are investigated on problems of linear elasticity and eigenfrequency analysis in 2D. In particular, focus is put on non-uniform rational B-spline patches which join nonconformingly along their common interface. Thus, the application of isogeometric analysis is extended to multi-patches, which can have an arbitrary parametrization on the adjacent edges. Moreover, it has been shown that the unique properties provided by isogeometric analysis, that is, high-order functions and smoothness across the element boundaries, carry over for the analysis of multiple domains. Copyright © 2013 John Wiley & Sons, Ltd.

Received 23 April 2013; Revised 7 August 2013; Accepted 8 August 2013

KEY WORDS: domain decomposition methods; isogeometric analysis; nonconforming NURBS multi-patches; Nitsche-type formulation

1. INTRODUCTION

The analysis of physical phenomena requires numerical methods that provide highly accurate results in an efficient way and that are optimally converging. All these attributes are contained in the context of isogeometric analysis (IGA). IGA was proposed in [1]. It uses a geometric basis, as used in computer-aided geometric design, within the analysis process. In its original version, non-uniform rational B-splines (NURBS) are employed because they are the predominant technology in geometric modeling. Within this paper, these functions are used as well. Nevertheless, other geometric bases such as polynomial splines over hierarchical T-meshes, subdivision surfaces, or T-splines can be used as well, as it has been demonstrated in [2–7]. Consequently, the usual transition from the geometric model to the analysis model via meshing in the standard FEMs can be avoided. The advantages coming along are exactness of the geometric model throughout any refinement level and efficiency as no time is spent in preparing the analysis model, see for example [8]. By using IGA for the analysis on complex geometric models, multiple patches have to be considered because a single NURBS patch cannot represent geometries of arbitrary complexity, on account of its tensor product nature. In particular, the multi-patches under consideration might be the result of the trimming of an initial NURBS patch [9]. Moreover, these multi-patches do not necessarily join conformingly at their common boundaries. In the context of IGA, mostly matching parametrizations have been discussed so far. For shell problems, an explicit formulation of the interface constraint

*Correspondence to: Andreas Apostolatos, Lehrstuhl für Statik, Technische Universität München, Arcisstrasse 21, D-80333, Munich, Bavaria, Germany.

†E-mail: andreas.apostolatos@tum.de

has been proposed in [10]. This approach is restricted into smooth patch transition cases. In [11], the so-called bending strip method extended this coupling approach into several multi-patches that join with arbitrary angles at their common interface. A mortar method was firstly introduced in [12] in the analysis of 3D elasticity problems and in [13] in the context of contact problems.

Within this paper, the *domain decomposition methods* (DDMs) are employed for the solution of BVPs in multiple domains, see for instance [14]. These methods can be applied in problems that involve different physics at each subdomain, for example, fluid–structure interaction [15–19] and in problems comprising several subdomains with the same underlying physics, for example, contact mechanics [20, 21]. Another field of application of the DDMs is parallel computing [22], where the domain is decomposed out of computational reasons and not because of problem setting itself. Generally, the DDMs can be distinguished into overlapping and non-overlapping. As the names imply, in the overlapping DDMs, the subdomains do overlap, whereas in the non-overlapping DDMs, they do not. In this contribution, the family of non-overlapping DDMs is applied in combination with IGA. Herein, the geometric exactness and the high-order functions of the IGA method are exploited. In particular, four main DDMs are discussed in detail: the *penalty*, the *Lagrange multiplier*, the *augmented Lagrange multiplier*, and a *Nitsche*-type method.

The penalty method, see for instance [23] or [24], enjoys great popularity in practice because of its simple implementation, and in that, the size of the equation system remains unaltered. A uniform convergence to the solution can only be guaranteed if the involved penalty parameter is increased with the refinement level. The drawback of the latter attribute is that the equation system becomes rapidly ill-conditioned. Typically, the penalty parameter needs to be set constant. This in turn has the implication that a certain amount of the error remains, independently of the refinement level.

The Lagrange multiplier approach [25] makes use of an additional field to guarantee the satisfaction of the interface constraints. For problems in mechanics, this field can be interpreted as the tractions on the interface. Hence, the Lagrange multiplier is a mixed formulation because both displacements and tractions are the solution of the resulting system. For the case of nonconforming meshes, this method is often denoted as the *mortar FEM* [26]. In this case, the problem, one is solving for, is a saddle point problem. This poses restrictions on the chosen finite dimensional spaces for obtaining a stable formulation and for ensuring uniqueness of the weak solution. Functions satisfying the so-called Ladyženskaja-Babuška-Brezzi condition attain these properties, refer to [27]. For an arbitrary set of basis functions, this condition cannot be satisfied and typically leads into oscillatory results [28]. Nevertheless, in the scope of this study, the Lagrange multiplier method has proved to be satisfactorily accurate. For elasticity problems, it is possible to condense out the Lagrange multipliers from the discrete equation system and thus eliminate its saddle point nature. This can be realized by solving iteratively the interface problem related to the Lagrange multipliers, by using the finite element tearing and interconnecting method, as proposed in [29]. In [30], this method has been extended in the case of IGA for its application to the joint analysis of nonconforming NURBS multi-patches, abbreviated as isogeometric tearing and interconnecting.

The augmented Lagrange multiplier method [31] is a combination of the penalty and the Lagrange multiplier methods. This method demonstrates higher accuracy than the Lagrange multiplier because of the penalty contributions. Additionally, the penalty parameter does not have to tend to infinity in order to obtain a uniform convergence, as in the penalty method. On the other hand, the problem is still a saddle point problem. Thus, the same restrictions as for the Lagrange multiplier also apply in the augmented Lagrange multiplier approach.

In its original version, the Nitsche method, see [32], is a method to impose Dirichlet boundary conditions in a weak sense for BVPs. In [33], the authors proposed a weak imposition of essential boundary conditions formulation based on the Nitsche idea for the convection–diffusion, fluid mechanics, and turbulence problems. The formulation resulted in a significant increase in the solution accuracy for this class of problems, both in the boundary layers and in the domain interior. Weakly enforced boundary conditions are now routinely employed for very high Reynolds number flows in wind turbine aerodynamics and fluid–structure interaction computations [34, 35], as well as in free-surface fluid-object interaction ship hydrodynamics simulations [36, 37]. In [38], this approach was extended to the solution of elliptic problems in the case of non-matching grids. In terms of IGA, the Nitsche method was firstly employed in [39] to weakly impose Dirichlet boundary

conditions. This paper presents a Nitsche-type formulation for nonconforming patches in the context of IGA. The main advantages of the proposed method is the positive definiteness of the resulting linear equation system and the uniform convergence to the solution. This is achieved by stabilizing the formulation using a penalty-like term. The related stabilization parameter is mesh-dependent and can be obtained by the solution of a generalized eigenvalue problem over the interface DOFs, as proposed in [40]. Among other positive features are that the stabilization parameter remains finite and that the size of the equation system remains unchanged. Alternatively, to solving the eigenvalue problem, the penalty parameter may be defined using appropriate scaling with the local mesh size and material parameters. The multiplicative constant in front of the penalty parameter may be computed from the element-level inverse estimate [33] and depends only on the element type and polynomial order. As a result, the weak imposition of the essential boundary conditions may alternatively be implemented without solving the interface eigenvalue problem, which further reduces the cost.

The outline of the paper is as follows. At first, the strong formulation of the BVP and the corresponding variational formulations for each DDM are given in Section 2 as a basis for the development and discussion of the corresponding solution procedures. All the variational formulations are provided in a unified notation to enable a clear and a comprehensive comparison between them. In Section 3, the discrete counterparts of the variational formulations are elaborated. Additionally, the computation of an estimation for the stabilization parameter in the Nitsche approach is delineated. The next section, Section 4, provides a numerical assessment of the individual DDMs for nonconforming multi-patch structures in IGA. This covers 2D linear elastic boundary value and eigenvalue problems. The methodologies are evaluated on elasticity problems, for which analytical solutions in displacements and stresses are available. This forms the basis for a comprehensive study. For the eigenfrequency analysis problems the multi-patch solutions are compared with single patch solutions. The numerical results show that the combination of the DDMs with IGA is highly beneficial for both studied problems in terms of accuracy, computational efficiency and robustness.

2. THEORY

2.1. The strong form of the problem

The model problem is an elastic body $\overline{\Omega}$ in a 2D plane stress analysis. It is assumed that the domain Ω is an open subset of the Euclidean space \mathbb{R}^2 with a piecewise C^1 -continuous boundary $\partial\Omega = \Gamma$ such that the unit vector normal to the boundary can be uniquely defined almost everywhere on Γ . For each material particle $(X^1, X^2) = \mathbf{X} \in \overline{\Omega}$ and at each time instance t , the unknown displacement field $\mathbf{u} = \mathbf{u}(\mathbf{X}; t)$ is defined in a Lagrangian description of the motion. The time domain is assumed to be the closed interval $\mathbb{T} = [0, T] \subset \mathbb{R}$, T being the end time of the dynamical process. The body $\overline{\Omega}$ is fixed along a portion of its boundary $\Gamma_d \subset \Gamma$, assuming $\mathbf{u} = \mathbf{g} = \mathbf{0}$ on Γ_d and thus confining the investigation into the homogeneous Dirichlet boundary conditions without loss of generality. However, extension of the methods to account also for inhomogeneous Dirichlet boundary conditions is straightforward. Additionally, tractions \mathbf{q} are prescribed along another portion of its boundary $\Gamma_n \subset \Gamma$, with $\Gamma_d \cap \Gamma_n = \emptyset$. Let \mathfrak{S}^m denote the space of all m^{th} order symmetric tensors. The strain field $\boldsymbol{\varepsilon} \in \mathfrak{S}^2$ is defined as the symmetric part of the displacement gradient field, namely,

$$\boldsymbol{\varepsilon}(\mathbf{u}) := \frac{1}{2} (\nabla \mathbf{u} + (\nabla \mathbf{u})^T) \quad \text{in } \overline{\Omega}. \quad (1)$$

Subsequently, it is also assumed that the stress field $\boldsymbol{\sigma} \in \mathfrak{S}^2$ is depending linearly on the strain field through Hooke's law [41]:

$$\boldsymbol{\sigma}(\mathbf{u}) = \tilde{\mathbf{C}} : \boldsymbol{\varepsilon}(\mathbf{u}) \quad \text{in } \overline{\Omega}, \quad (2)$$

$\tilde{\mathbf{C}} \in \mathfrak{S}^4$ being the elasticity tensor. This study is confined into 2D elasticity problems. The assumption coming along is that the mechanical reaction of the body is restricted into the X^1 - X^2 plane,

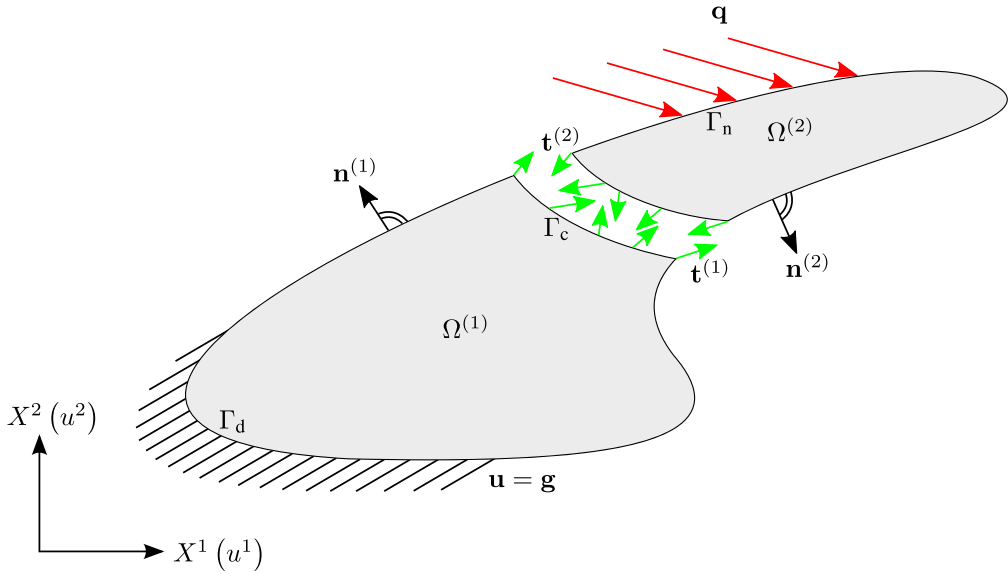


Figure 1. The decomposed BVP into two subdomains.

whereas the stress tensor σ varies constantly in the lateral to X^1 - X^2 direction, namely, the thickness direction denoted by h . Then, the problem is fully characterized by the resultant force tensor $\mathbf{p} = \sigma h$. Consequently, the material law (2) in this case may be alternatively defined as

$$\mathbf{p}(\mathbf{u}) = \mathbf{C} : \boldsymbol{\varepsilon}(\mathbf{u}) \quad \text{in } \overline{\Omega}, \quad (3)$$

where $\mathbf{C} = \frac{1}{h} \widetilde{\mathbf{C}}$ denotes the particular elasticity tensor for the plane elasticity problems, for example, plane stress or plane strain problems. The domain Ω is decomposed into two open subsets $\Omega^{(1)}$ and $\Omega^{(2)}$ for which the following relations hold:

$$\bigcup_{\alpha=1}^2 \overline{\Omega}^{(\alpha)} = \overline{\Omega} \text{ and } \bigcap_{\alpha=1}^2 \overline{\Omega}^{(\alpha)} = \overline{\Gamma}_c, \quad (4)$$

Γ_c being a piecewise C^1 -continuous curve on the 2D Euclidean space in the context of the non-overlapping DDMs, which are the subject of this study. The Dirichlet and the Neumann boundaries, Γ_d and Γ_n respectively, are decomposed in the same fashion as Ω in (4). The aforementioned problem is depicted in Figure 1. Subsequently, it is also assumed that the displacement, the resultant force, and the traction fields are defined piecewisely in $\overline{\Omega}$ at each subdomain $\overline{\Omega}^{(\alpha)}$. Whenever the displacement, the resultant force, or the traction field is restricted into one subdomain, a superscript $\alpha = 1, 2$ is used to indicate the domain of restriction, that is, $\mathbf{u}|_{\overline{\Omega}^{(\alpha)}} = \mathbf{u}^{(\alpha)}$, $\mathbf{p}(\mathbf{u}^{(\alpha)}) = \mathbf{p}^{(\alpha)}$, and $\mathbf{t}(\mathbf{u}^{(\alpha)}) = \mathbf{t}^{(\alpha)}$, respectively. Then, the plane elasticity of two domain decomposed initial BVP writes [42]

$$\rho \ddot{\mathbf{u}} + \nabla \cdot \mathbf{p} + \mathbf{b} = \mathbf{0} \quad , \quad \text{in } \Omega \setminus \Gamma_c \times \mathbb{T}, \quad (5a)$$

$$\mathbf{u} = \mathbf{g} \quad , \quad \text{on } \Gamma_d \times \mathbb{T}, \quad (5b)$$

$$\mathbf{u}(t=0) = \mathbf{u}_0 \quad , \quad \text{in } \Omega, \quad (5c)$$

$$\dot{\mathbf{u}}(t=0) = \mathbf{v}_0 \quad , \quad \text{in } \Omega, \quad (5d)$$

$$\mathbf{t} = \mathbf{q} \quad , \quad \text{on } \Gamma_n \times \mathbb{T}, \quad (5e)$$

$$\mathbf{u}^{(1)} - \mathbf{u}^{(2)} = \mathbf{0} \quad , \quad \text{on } \Gamma_c \times \mathbb{T}, \quad (5f)$$

$$\mathbf{t}^{(1)} + \mathbf{t}^{(2)} = \mathbf{0} \quad , \quad \text{on } \Gamma_c \times \mathbb{T}, \quad (5g)$$

where ρ and $\ddot{\mathbf{u}}$ are the material density and the acceleration field, respectively. Additionally, \mathbf{u}_0 and \mathbf{v}_0 denote the initial conditions for the displacement and the velocity field, respectively. Then, \mathbf{t} and $\mathbf{t}^{(\alpha)}$ denote the traction forces at the boundaries $\partial\Omega$ and $\partial\Omega^{(\alpha)}$, namely, $\mathbf{t} = \mathbf{p} \cdot \mathbf{n}$ and $\mathbf{t}^{(\alpha)} = \mathbf{p}^{(\alpha)} \cdot \mathbf{n}^{(\alpha)}$. Additionally, \mathbf{n} and $\mathbf{n}^{(\alpha)}$ are the unit normal to the boundaries $\partial\Omega$ and $\partial\Omega^{(\alpha)}$ vectors, as can be seen in Figure 1. Equations (5f) and (5g) represent the Dirichlet and the Neumann interface conditions, respectively. Those equations ensure the pointwise compatibility of the solution and the equilibrium across the interface Γ_c .

2.2. The weak form of the decoupled system

Let us introduce the subspace of $(H^1(\Omega^{(1)} \cup \Omega^{(2)}))^2$ needed for the weak equilibrium equation of the decomposed plane elasticity BVP, namely,

$$\mathcal{V} = \left\{ \mathbf{v} \in \left(H^1(\Omega^{(1)} \cup \Omega^{(2)}) \right)^2 \mid \mathbf{v} = \mathbf{0} \text{ on } \Gamma_d \right\}. \quad (6)$$

The variational formulation of the initial BVP (5a)–(5g) without consideration of the interface conditions is written as follows [41]: Find $\mathbf{u} \in \mathcal{V}$ such that

$$\langle \rho \ddot{\mathbf{u}}, \mathbf{v} \rangle_{0,\Omega} + a(\mathbf{u}, \mathbf{v}) = L(\mathbf{v}) \quad \forall \mathbf{v} \in \mathcal{V}. \quad (7)$$

The notation $\langle \cdot, \cdot \rangle_{0,\Omega}$ stands for the inner product in the $L^2(\Omega)$ space. Therefore, the first term in Equation (7) is interpreted as

$$\langle \rho \ddot{\mathbf{u}}, \mathbf{v} \rangle_{0,\Omega} = \int_{\Omega} \rho \ddot{\mathbf{u}} \cdot \mathbf{v} \, d\Omega. \quad (8)$$

The bilinear form $a : \mathcal{V} \times \mathcal{V} \rightarrow \mathbb{R}$ and the linear functional $L : \mathcal{V} \rightarrow \mathbb{R}$, which appear in (7), are defined as follows:

$$a(\mathbf{u}, \mathbf{v}) := \sum_{\alpha=1}^2 \int_{\Omega^{(\alpha)}} \boldsymbol{\epsilon}(\mathbf{u}^{(\alpha)}) : \mathbf{C} : \boldsymbol{\epsilon}(\mathbf{v}^{(\alpha)}) \, d\Omega, \quad (9a)$$

$$L(\mathbf{v}) := \sum_{\alpha=1}^2 \left(\int_{\Omega^{(\alpha)}} \mathbf{b} \cdot \mathbf{v}^{(\alpha)} \, d\Omega + \int_{\Gamma_n^{(\alpha)}} \mathbf{q} \cdot \mathbf{v}^{(\alpha)} \, d\Gamma \right). \quad (9b)$$

Because compatibility of the solution between the subdomains over Γ_c is required only in the stiffness of the mechanical system, the inertial contributions in variational formulation (7) can be neglected for the detailed development of the DDMs on the basis of their individual formulations. Then, once the DDM variational formulations have been developed for the steady-state case, they can be extended with the inertial terms without significant effort. Equation (7) represents the equilibrium at each subdomain $\Omega^{(\alpha)}$ but does not account for the compatibility of the solutions $\mathbf{u}^{(\alpha)}$ across the interface. The compatibility of the solution across Γ_c is achieved using the DDMs in a weak sense, which is discussed in the forthcoming sections.

2.3. The weak form of the penalty approach

Let us introduce the space $\mathfrak{L} \subset \mathcal{V}$, namely,

$$\mathfrak{L} := \left\{ \mathbf{v} \in \mathcal{V} \mid \exists \text{ c.e. } \mathbf{v}^{(\alpha)} \text{ on } \Gamma_c \text{ such that } \mathbf{v}^{(1)} - \mathbf{v}^{(2)} \in (L^2(\Gamma_c))^2 \right\}, \quad (10)$$

where the designation c.e. stands for continuous extension(s). To account for the coupling in the penalty approach, the interface Dirichlet condition (5f) is weighted with its test counterpart, multiplied with a penalty parameter $\frac{\bar{\alpha}}{2}$, and added to the steady-state version of (7). In this way, one obtains the variational formulation of the problem using the penalty approach, namely, find $\mathbf{u} \in \mathfrak{L}$ with $\mathbf{u}^{(1)} - \mathbf{u}^{(2)} = \chi$ on Γ_c such that

$$a(\mathbf{u}, \mathbf{v}) + \frac{\bar{\alpha}}{2} \langle \chi, \psi \rangle_{0,\Gamma_c} = L(\mathbf{v}), \quad (11)$$

for all $\mathbf{v} \in \mathfrak{L}$ with $\mathbf{v}^{(1)} - \mathbf{v}^{(2)} = \boldsymbol{\psi}$ on Γ_c . The penalty method is often called variationally inconsistent in that one cannot recover the interface conditions of the strong form (5a)–(5g) by using the weak form (11). Additionally, it is important to note that the accuracy of the method depends on the choice of the penalty parameter. Typically, small values for $\bar{\alpha}$ do not yield satisfactory results in terms of the interface compatibility constraints, whereas too large values for $\bar{\alpha}$ result in ill-conditioned discrete equation systems. In addition, the penalty method demonstrates convergence up to a certain refinement level where it levels off for a fixed penalty factor. The leveling off point depends on the magnitude of the penalty parameter, a statement that can be strictly justified through the error estimates developed in [23].

2.4. The weak form of the Lagrange multiplier approach

In the context of the Lagrange multiplier formulation, an additional field is considered, the so-called Lagrange multiplier field, denoted by λ . The interface Neumann condition (5g) can be re-written as follows:

$$\mathbf{t}^{(1)} = \mathbf{p}^{(1)} \cdot \mathbf{n}^{(1)} = -\lambda , \quad (12a)$$

$$\mathbf{t}^{(2)} = \mathbf{p}^{(2)} \cdot \mathbf{n}^{(2)} = \lambda , \quad (12b)$$

thus including the additional unknown field $\lambda \in C^{-1}(\Gamma_c)$ into the strong form of the problem. Then, the right-hand side of the weak equilibrium equation (7) without the inertial contributions is enriched with additional work terms accounting for the work performed by the Lagrange multiplier field on Γ_c . Subsequently, one multiplies the interface Dirichlet condition (5f) with a $\mu \in (L^2(\Gamma_c))^2$, integrates over Γ_c , and sums up the resulting integral equation to the weak equilibrium equation. Hence, the complete Lagrange multiplier formulation is written as follows: Find $\mathbf{u} \in \mathfrak{L}$ with $\mathbf{u}^{(1)} - \mathbf{u}^{(2)} = \chi$ on Γ_c and $\lambda \in (L^2(\Gamma_c))^2$ such that

$$a(\mathbf{u}, \mathbf{v}) + \langle \lambda, \boldsymbol{\psi} \rangle_{0, \Gamma_c} + \langle \chi, \mu \rangle_{0, \Gamma_c} = L(\mathbf{v}) , \quad (13)$$

for all $\mathbf{v} \in \mathfrak{L}$ with $\mathbf{v}^{(1)} - \mathbf{v}^{(2)} = \boldsymbol{\psi}$ on Γ_c and for all $\mu \in (L^2(\Gamma_c))^2$. The weak solution of the Lagrange multiplier formulation is restricted into $\mathcal{V}_L := \mathfrak{L} \times (L^2(\Gamma_c))^2$. Hence, the variational formulation (13) represents a saddle point problem meaning that within its discretized form, the chosen finite dimensional spaces must satisfy the inf-sup (Ladyženskaja-Babuška-Brezzi) condition, such that a unique solution to the problem can be guaranteed.

2.5. The weak form of the augmented Lagrange multiplier approach

The augmented Lagrange multiplier approach of the problem is obtained as a combination of the Lagrange multiplier and the penalty formulations, namely, find $\mathbf{u} \in \mathfrak{L}$ with $\mathbf{u}^{(1)} - \mathbf{u}^{(2)} = \chi$ on Γ_c and $\lambda \in (L^2(\Gamma_c))^2$ such that

$$a(\mathbf{u}, \mathbf{v}) + \langle \lambda, \boldsymbol{\psi} \rangle_{0, \Gamma_c} + \frac{\bar{\alpha}}{2} \langle \chi, \boldsymbol{\psi} \rangle_{0, \Gamma_c} + \langle \chi, \mu \rangle_{0, \Gamma_c} = L(\mathbf{v}) , \quad (14)$$

for all $\mathbf{v} \in \mathfrak{L}$ with $\mathbf{v}^{(1)} - \mathbf{v}^{(2)} = \boldsymbol{\psi}$ on Γ_c and for all $\mu \in (L^2(\Gamma_c))^2$. The weak solution of the augmented Lagrange multiplier approach is also restricted into \mathcal{V}_L , meaning that formulation (14) is also a saddle point problem. The idea is that the accuracy of the Lagrange multiplier method is improved by the penalty terms in that the error in the Dirichlet interface constraint is controlled by the penalty parameter. Moreover, that penalty parameter does not have to tend to infinity such that a uniform convergence can be achieved.

2.6. The weak form of the Nitsche approach

In this section, a Nitsche-type formulation of the decomposed plane elasticity problem is derived. The method is based on the weak enforcement of the Neumann interface condition (5g) into the variational formulation. The variational formulation of the Nitsche method must be enriched with

a stabilization term such that the Nitsche bilinear form remains coercive. An estimation of this stabilization parameter can be obtained from the solution of a generalized eigenvalue problem over the interface.

2.6.1. The variational formulation. In the context of the Nitsche approach, it is necessary to define the mean interface resultant force field $\bar{\mathbf{p}} : \mathcal{V} \times \mathcal{V} \rightarrow \mathfrak{S}^2$, namely,

$$\bar{\mathbf{p}}(\mathbf{v}, \mathbf{w}) := (1 - \gamma)\mathbf{p}(\mathbf{v}) + \gamma\mathbf{p}(\mathbf{w}) \quad \text{on } \Gamma_c, \quad (15)$$

for all $\mathbf{v}, \mathbf{w} \in \mathcal{V}$ independent displacement fields and $\gamma \in [0, 1]$ being a free parameter. This accounts for the weighting of the solution on the interface, and hence, its choice in the closed interval $[0, 1]$ is free. Also, note that if both arguments of $\bar{\mathbf{p}}$ are restricted in one of the domains $\Omega^{(\alpha)} \cup \Gamma_c$, the mean interface resultant force field reduces to the resultant force field of that subdomain meaning $\bar{\mathbf{p}}(\mathbf{u}^{(\alpha)}, \mathbf{u}^{(\alpha)}) = \mathbf{p}^{(\alpha)}$. Thus, $\bar{\mathbf{p}}$ is an extension of the resultant force field from each subdomain $\Omega^{(\alpha)}$ on the interface Γ_c . The space $\mathfrak{N} \subset \mathcal{V}$ is also to be defined in this section, namely,

$$\mathfrak{N} := \left\{ \mathbf{v} \in \mathcal{V} \mid \exists \text{ c.e. } \mathbf{v}^{(\alpha)} \text{ on } \Gamma_c \text{ such that } \bar{\mathbf{p}}(\mathbf{v}^{(1)}, \mathbf{v}^{(2)}) \cdot \mathbf{n}^{(1)} \in (L^2(\Gamma_c))^2 \right\}. \quad (16)$$

The weak solution of the Nitsche formulation is then restricted into $\mathcal{V}_N := \mathfrak{L} \cup \mathfrak{N}$. Extending the linear functional in the steady-state version of Equation (7) to account also for the interface work contributions and by also using the Neumann interface condition (5g), one obtains the following variational formulation of the problem: Find $\mathbf{u} \in \mathcal{V}_N$ with $\mathbf{u}^{(1)} - \mathbf{u}^{(2)} = \chi$ and $\bar{\mathbf{p}}(\mathbf{u}^{(1)}, \mathbf{u}^{(2)}) \cdot \mathbf{n}^{(1)} = \xi$ on Γ_c such that

$$a(\mathbf{u}, \mathbf{v}) - \langle \xi, \psi \rangle_{0, \Gamma_c} - \langle \chi, \zeta \rangle_{0, \Gamma_c} = L(\mathbf{v}), \quad (17)$$

for all $\mathbf{v} \in \mathcal{V}_N$ with $\mathbf{v}^{(1)} - \mathbf{v}^{(2)} = \psi$ and $\bar{\mathbf{p}}(\mathbf{v}^{(1)}, \mathbf{v}^{(2)}) \cdot \mathbf{n}^{(1)} = \zeta$ on Γ_c . Unfortunately, the Nitsche bilinear form $a_N : \mathcal{V}_N \times \mathcal{V}_N \rightarrow \mathbb{R}$ in the left-hand side of (17), namely,

$$a_N(\mathbf{u}, \mathbf{v}) := a(\mathbf{u}, \mathbf{v}) - \langle \xi, \psi \rangle_{0, \Gamma_c} - \langle \chi, \zeta \rangle_{0, \Gamma_c}, \quad (18)$$

is not coercive because of the mixed terms. This has the implication that one unique solution cannot be guaranteed, which in turn means that the resulting discrete equation system involves a non-positive definite system matrix.

2.6.2. Stabilization of the formulation. In order to obtain a coercive bilinear form, the form (18) is extended with a stabilization term. Then, the extended bilinear form $\bar{a}_N : \mathcal{V}_N \times \mathcal{V}_N \rightarrow \mathbb{R}$, writes

$$\bar{a}_N(\mathbf{u}, \mathbf{v}) := a(\mathbf{u}, \mathbf{v}) - \langle \xi, \psi \rangle_{0, \Gamma_c} - \langle \chi, \zeta \rangle_{0, \Gamma_c} + \beta \langle \chi, \psi \rangle_{0, \Gamma_c}. \quad (19)$$

The meaning of the symbols in (19) is the same as in Equation (18), and β denotes the stabilization parameter. In this way, the stabilized variational formulation of the problem using the Nitsche approach is written as follows: Find $\mathbf{u} \in \mathcal{V}_N$ with $\mathbf{u}^{(1)} - \mathbf{u}^{(2)} = \chi$ and $\bar{\mathbf{p}}(\mathbf{u}^{(1)}, \mathbf{u}^{(2)}) \cdot \mathbf{n}^{(1)} = \xi$ on Γ_c such that

$$a(\mathbf{u}, \mathbf{v}) - \langle \xi, \psi \rangle_{0, \Gamma_c} - \langle \chi, \zeta \rangle_{0, \Gamma_c} + \beta \langle \chi, \psi \rangle_{0, \Gamma_c} = L(\mathbf{v}), \quad (20)$$

for all $\mathbf{v} \in \mathcal{V}_N$ with $\mathbf{v}^{(1)} - \mathbf{v}^{(2)} = \psi$ and $\bar{\mathbf{p}}(\mathbf{v}^{(1)}, \mathbf{v}^{(2)}) \cdot \mathbf{n}^{(1)} = \zeta$ on Γ_c . It can be shown that there exists an interval of choice for the stabilization parameter β such that the bilinear form \bar{a}_N is coercive, which is provided thereafter.

Proposition 2.1. The extended Nitsche form defined in (19) is coercive if the stabilization parameter is chosen as $\beta \geq 2c^2$ where $c > 0$ is the constant of the following inequality:

$$\left\| \bar{\mathbf{p}}(\mathbf{v}^{(1)}, \mathbf{v}^{(2)}) \cdot \mathbf{n}^{(1)} \right\|_{0, \Gamma_c} \leq c (a(\mathbf{v}, \mathbf{v}))^{\frac{1}{2}}, \quad (21)$$

for all test functions $\mathbf{v} \in \mathcal{V}$.

Proposition 2.1 follows closely Equation (1.9) in the original document [40]. In that study, the Nitsche approach has been developed for the application of Dirichlet boundary conditions in the partition of unity method [43]. Then, discretization of inequality (21) yields a generalized eigenvalue problem over the interface. The largest eigenvalue of the latter mentioned system can be chosen as an approximation of the constant c , providing a suitable estimation for the stabilization parameter β .

3. DISCRETIZATION

3.1. Discrete form of the steady-state problem

The method of choice for the study within this paper is IGA, as mentioned in the Introduction. Because the isoparametric concept is an essential part of IGA, the finite dimensional subspaces for \mathcal{V} and $(L^2(\Gamma_c))^2$ are chosen to comply with the NURBS space of the geometry parametrization. Let $\mathcal{T}_h = (\mathcal{T}_i)_i$ with $\dim \mathcal{T}_h = n$ and $\mathcal{T}_i^\lambda = (\mathcal{T}_i^\lambda)_i$ with $\dim \mathcal{T}_i^\lambda = n_\lambda$ be triangulations of $\overline{\Omega}$ and $\overline{\Gamma}_c$ respectively, which are compatible with the decomposition of $\overline{\Omega}$ and $\overline{\Gamma}_c$ into finite elements. Let in addition \mathcal{T}_i and \mathcal{T}_j^λ to be open sets for every $i = 1, \dots, n$ and every $j = 1, \dots, n_\lambda$. Those sets are also assumed to satisfy the following conditions:

$$\mathcal{T}_i \cap \mathcal{T}_j = \emptyset \quad \forall \mathcal{T}_i, \mathcal{T}_j \in \mathcal{T}_h \text{ with } i \neq j , \quad (22a)$$

$$\mathcal{T}_i^\lambda \cap \mathcal{T}_j^\lambda = \emptyset \quad \forall \mathcal{T}_i^\lambda, \mathcal{T}_j^\lambda \in \mathcal{T}_h^\lambda \text{ with } i \neq j , \quad (22b)$$

$$\bigcup_{i=1}^n \overline{\mathcal{T}}_i = \overline{\Omega} , \quad (22c)$$

$$\bigcup_{i=1}^{n_\lambda} \overline{\mathcal{T}}_i^\lambda = \overline{\Gamma}_c . \quad (22d)$$

In the context of IGA, the finite dimensional subspaces $\mathcal{V}_h \subset \mathcal{V}$ and $\mathcal{V}_h^\lambda \subset (L^2(\Gamma_c))^2$ are defined as follows:

$$\mathcal{V}_h := \left\{ \mathbf{v} \in \mathcal{V} \mid \mathbf{v} \in (\mathcal{R}(\mathcal{T}_i))^2 \text{ for every } \mathcal{T}_i \in \mathcal{T}_h \right\} , \quad (23a)$$

$$\mathcal{V}_h^\lambda := \left\{ \boldsymbol{\lambda} \in (L^2(\Gamma_c))^2 \mid \boldsymbol{\lambda} \in (\mathcal{R}(\mathcal{T}_i^\lambda))^2 \text{ for every } \mathcal{T}_i^\lambda \in \mathcal{T}_h^\lambda \right\} , \quad (23b)$$

$\mathcal{R}(\mathcal{T}_i)$ being the space of all rational polynomials in the set \mathcal{T}_i . It is now clear that the dimension of \mathcal{V}_h and \mathcal{V}_h^λ is $\dim \mathcal{V}_h = 2n$ and $\dim \mathcal{V}_h^\lambda = 2n_\lambda$, respectively. Let $\Phi = (\phi_1, \dots, \phi_{2n})$ and $\Phi^\lambda = (\phi_1^\lambda, \dots, \phi_{2n_\lambda}^\lambda)$ be bases of \mathcal{V}_h and \mathcal{V}_h^λ , respectively. Then, it follows that for every elements $\mathbf{v}_h \in \mathcal{V}_h$ and $\boldsymbol{\lambda}_h \in \mathcal{V}_h^\lambda$ there exist reals \hat{v}_i and $\hat{\lambda}_i$ such that

$$\mathbf{v}_h = \sum_{i=1}^{2n} \phi_i \hat{v}_i , \quad (24a)$$

$$\boldsymbol{\lambda}_h = \sum_{i=1}^{2n_\lambda} \phi_i^\lambda \hat{\lambda}_i . \quad (24b)$$

The hat in the discrete scalar values reflects to the fact that those attain, in general, no direct physical interpretation because of the non-interpolatory nature of the NURBS basis functions as opposed to

classical FEMs, see [44]. In this way, one can define the discrete spaces for the displacement and the Lagrange multiplier fields as follows:

$$\mathcal{K} := \left\{ (\hat{v}_i)_{i=1}^{2n} = \hat{\mathbf{v}} \in \mathbb{R}^{2n} \mid \sum_{i=1}^{2n} \phi_i \hat{v}_i \in \mathcal{V}_h \right\}, \quad (25a)$$

$$\mathcal{K}_\lambda := \left\{ (\hat{\lambda}_i)_{i=1}^{2n_\lambda} = \hat{\lambda} \in \mathbb{R}^{2n_\lambda} \mid \sum_{i=1}^{2n_\lambda} \phi_i^\lambda \hat{\lambda}_i \in \mathcal{V}_h^\lambda \right\}. \quad (25b)$$

For all variational formulations of the DDMs, the only requirement for the jump of the solution across the interface Γ_c is $\mathbf{u}^{(1)} - \mathbf{u}^{(2)} \in (L^2(\Gamma_c))^2$, see equations (11), (13), (14), and (20) for the penalty, the Lagrange multiplier, the augmented Lagrange multiplier, and the Nitsche formulation, respectively. This in turn means that the basis to construct \mathcal{V}_h can also be discontinuous and square integrable across Γ_c . Thus, Φ can be decomposed as follows:

$$\Phi = \bigcup_{\alpha=1}^2 \Phi^{(\alpha)}, \quad (26)$$

where $\Phi^{(\alpha)} = (\phi_1^{(\alpha)}, \dots, \phi_{2n^{(\alpha)}}^{(\alpha)})$ with $\dim \Phi^{(\alpha)} = 2n^{(\alpha)}$ and $n^{(1)} + n^{(2)} = n$. This justification allows for modeling the subdomains with distinct NURBS patches each of which to attain its own geometric basis. Let the complete vector of DOFs to be $[\hat{\mathbf{u}}^{(1)} \quad \hat{\mathbf{u}}^{(2)}]^T = \hat{\mathbf{u}} \in \mathcal{K}$, where $\hat{\mathbf{u}}^{(\alpha)}$ stands for the DOFs related to each subdomain. Projection of the bilinear form (9a) and the linear functional (9b) onto $\mathcal{V}_h \times \mathcal{V}_h$ and \mathcal{V}_h respectively and substitution in the steady-state version of equation (7) yields the following discrete equation system:

$$\begin{bmatrix} \mathbf{K}^{(1)} & \mathbf{0} \\ \mathbf{0} & \mathbf{K}^{(2)} \end{bmatrix} \hat{\mathbf{u}} = \begin{bmatrix} \hat{\mathbf{F}}^{(1)} \\ \hat{\mathbf{F}}^{(2)} \end{bmatrix}. \quad (27)$$

In equation (27), $\mathbf{K}^{(\alpha)}$ and $\hat{\mathbf{F}}^{(\alpha)}$ denote the stiffness matrices and the load vectors at each subdomain, respectively. Note that equation system (27) represents two decoupled equation systems at each subdomain $\Omega^{(\alpha)}$. The coupling terms resulting from each DDM are discussed in the following sections.

3.2. Discrete equation system of the penalty approach

The projection of the bilinear form in the penalty approach $a_p : \mathfrak{L} \times \mathfrak{L} \rightarrow \mathbb{R}$, namely,

$$a_p(\mathbf{u}, \mathbf{v}) := a(\mathbf{u}, \mathbf{v}) + \frac{\bar{\alpha}}{2} \langle \chi, \psi \rangle_{0, \Gamma_c}, \quad (28)$$

onto $\mathcal{V}_h \times \mathcal{V}_h$ yields additional penalty stiffness and coupling matrices, $\mathbf{K}_p^{(\alpha)}$ and $\mathbf{C}_p^{(\alpha)}$, respectively, with entries

$$K_{p,i,j}^{(\alpha)} := \frac{\bar{\alpha}}{2} \langle \phi_i^{(\alpha)}, \phi_j^{(\alpha)} \rangle_{0, \Gamma_c}, \quad (29a)$$

$$C_{p,i,j}^{(1)} := -\frac{\bar{\alpha}}{2} \langle \phi_i^{(1)}, \phi_j^{(2)} \rangle_{0, \Gamma_c}, \quad (29b)$$

$$C_{p,i,j}^{(2)} := -\frac{\bar{\alpha}}{2} \langle \phi_i^{(2)}, \phi_j^{(1)} \rangle_{0, \Gamma_c}. \quad (29c)$$

By supplementing the equation system (27) with the penalty contributions, the discrete equation system for the penalty approach is written as follows: Find $\hat{\mathbf{u}} \in \mathcal{K}$ such that

$$\begin{bmatrix} \mathbf{K}^{(1)} + \mathbf{K}_p^{(1)} & \mathbf{C}_p^{(1)} \\ \mathbf{C}_p^{(2)} & \mathbf{K}^{(2)} + \mathbf{K}_p^{(2)} \end{bmatrix} \hat{\mathbf{u}} = \begin{bmatrix} \hat{\mathbf{F}}^{(1)} \\ \hat{\mathbf{F}}^{(2)} \end{bmatrix}, \quad (30)$$

Equation system (30) is always positive definite, property inherited from the fact that the bilinear form (28) is coercive [23].

3.3. Discrete equation system of the Lagrange multiplier approach

Projecting the left-hand side of Equation (13) onto $\mathcal{V}_h \times \mathcal{V}_h \times \mathcal{V}_h^\lambda$ supplies us with additional coupling matrices $\mathbf{C}_\lambda^{(\alpha)}$ related to the Lagrange multiplier field with entries

$$C_{\lambda,i,j}^{(\alpha)} := (-1)^{\alpha+1} \left\langle \phi_i^{(\alpha)}, \phi_j^\lambda \right\rangle_{0,\Gamma_c}. \quad (31)$$

In this way, the discrete equation system of the Lagrange multiplier approach is written as follows: Find $\hat{\mathbf{u}} \in \mathcal{K}$ and $\hat{\lambda} \in \mathcal{K}_\lambda$ such that

$$\begin{bmatrix} \mathbf{K}^{(1)} & \mathbf{0} & \mathbf{C}_\lambda^{(1)} \\ \mathbf{0} & \mathbf{K}^{(2)} & \mathbf{C}_\lambda^{(2)} \\ (\mathbf{C}_\lambda^{(1)})^T & (\mathbf{C}_\lambda^{(2)})^T & \mathbf{0} \end{bmatrix} \begin{bmatrix} \hat{\mathbf{u}} \\ \hat{\lambda} \end{bmatrix} = \begin{bmatrix} \hat{\mathbf{F}}^{(1)} \\ \hat{\mathbf{F}}^{(2)} \\ \mathbf{0} \end{bmatrix}, \quad (32)$$

where $\hat{\lambda} \in \mathcal{K}_\lambda$ is the vector of the DOFs for the Lagrange multiplier field. The existence of the zero block in the right bottom of the equation system (32) indicates that the Lagrange multiplier method yields a saddle point problem.

3.4. Discrete equation system of the augmented Lagrange multiplier approach

As discussed in Section 2.5, the augmented Lagrange multiplier approach is a combination of the Lagrange multiplier and the penalty approaches. Thus, its discrete equation system follows naturally the same structure, see Equations (32) and (30), namely, find $\hat{\mathbf{u}} \in \mathcal{K}$ and $\hat{\lambda} \in \mathcal{K}_\lambda$ such that

$$\begin{bmatrix} \mathbf{K}^{(1)} + \mathbf{K}_p^{(1)} & \mathbf{C}_p^{(1)} & \mathbf{C}_\lambda^{(1)} \\ \mathbf{C}_p^{(2)} & \mathbf{K}^{(2)} + \mathbf{K}_p^{(2)} & \mathbf{C}_\lambda^{(2)} \\ (\mathbf{C}_\lambda^{(1)})^T & (\mathbf{C}_\lambda^{(2)})^T & \mathbf{0} \end{bmatrix} \begin{bmatrix} \hat{\mathbf{u}} \\ \hat{\lambda} \end{bmatrix} = \begin{bmatrix} \hat{\mathbf{F}}^{(1)} \\ \hat{\mathbf{F}}^{(2)} \\ \mathbf{0} \end{bmatrix}. \quad (33)$$

Equation system (33) is of the same nature as (32), that is, a saddle point problem.

3.5. Discrete equation system of the Nitsche approach

Consequently, projecting the extended bilinear form of the Nitsche approach (19) onto $\mathcal{V}_h \times \mathcal{V}_h$ supplements the equation system (30) with the Nitsche stiffness and coupling matrices, $\mathbf{K}_N^{(\alpha)}$ and $\mathbf{C}_N^{(\alpha)}$ respectively, with entries

$$K_{N,i,j}^{(\alpha)} := (-1)^{\alpha+1} (\gamma + \alpha - 2) \left\langle \mathbf{p}(\phi_i^{(\alpha)}) \cdot \mathbf{n}^{(1)} + \phi_i^{(\alpha)}, \phi_j^{(\alpha)} + \mathbf{p}(\phi_j^{(\alpha)}) \cdot \mathbf{n}^{(1)} \right\rangle_{0,\Gamma_c}, \quad (34a)$$

$$C_{N,i,j}^{(1)} := \left\langle (1-\gamma) \mathbf{p}(\phi_i^{(1)}) \cdot \mathbf{n}^{(1)} + \gamma \phi_i^{(2)}, (1-\gamma) \phi_j^{(1)} + \gamma \mathbf{p}(\phi_j^{(2)}) \cdot \mathbf{n}^{(1)} \right\rangle_{0,\Gamma_c}, \quad (34b)$$

$$C_{N,i,j}^{(2)} := \left\langle \gamma \mathbf{p}(\phi_i^{(2)}) \cdot \mathbf{n}^{(1)} + (1-\gamma) \phi_i^{(1)}, \gamma \phi_j^{(2)} + (1-\gamma) \mathbf{p}(\phi_j^{(1)}) \cdot \mathbf{n}^{(1)} \right\rangle_{0,\Gamma_c}. \quad (34c)$$

In this way, the discrete equation system of the Nitsche approach is written as follows: Find $\hat{\mathbf{u}} \in \mathcal{K}$ such that

$$\begin{bmatrix} \mathbf{K}^{(1)} + \mathbf{K}_p^{(1)} + \mathbf{K}_N^{(1)} & \mathbf{C}_p^{(1)} + \mathbf{C}_N^{(1)} \\ \mathbf{C}_p^{(2)} + \mathbf{C}_N^{(2)} & \mathbf{K}^{(2)} + \mathbf{K}_p^{(2)} + \mathbf{K}_N^{(2)} \end{bmatrix} \hat{\mathbf{u}} = \begin{bmatrix} \hat{\mathbf{F}}^{(1)} \\ \hat{\mathbf{F}}^{(2)} \end{bmatrix}, \quad (35)$$

As already mentioned in Section 2.6.2, a generalized eigenvalue problem has to be solved over the interface DOFs $\hat{\mathbf{u}}_c = [\hat{\mathbf{u}}_c^{(1)} \quad \hat{\mathbf{u}}_c^{(2)}]^T$ in order to obtain an estimation of the stabilization parameter β . Discretizing inequality (21), the following eigenvalue problem occurs:

$$\begin{bmatrix} \mathbf{Q}_s^{(1)} & \mathbf{Q}_c^{(1)} \\ \mathbf{Q}_c^{(2)} & \mathbf{Q}_s^{(2)} \end{bmatrix} \hat{\mathbf{u}}_c = c_N^2 \begin{bmatrix} \mathbf{K}_{|\Gamma_c}^{(1)} & \mathbf{0} \\ \mathbf{0} & \mathbf{K}_{|\Gamma_c}^{(2)} \end{bmatrix} \hat{\mathbf{u}}_c, \quad (36)$$

where $\mathbf{K}_{|\Gamma_c}^{(\alpha)}$ denotes the restriction of the stiffness matrices on the interface DOFs, and the entries of the matrices $\mathbf{Q}_s^{(\alpha)}$ and $\mathbf{Q}_c^{(\alpha)}$ are given as follows:

$$Q_{s,i,j}^{(\alpha)} := \left\langle \mathbf{p}(\phi_i^{(\alpha)}) \cdot \mathbf{n}^{(1)}, \mathbf{p}(\phi_j^{(\alpha)}) \cdot \mathbf{n}^{(1)} \right\rangle_{0,\Gamma_c}, \quad (37a)$$

$$Q_{c,i,j}^{(1)} := \left\langle \mathbf{p}(\phi_i^{(1)}) \cdot \mathbf{n}^{(1)}, \mathbf{p}(\phi_j^{(2)}) \cdot \mathbf{n}^{(1)} \right\rangle_{0,\Gamma_c}, \quad (37b)$$

$$Q_{c,i,j}^{(2)} := \left\langle \mathbf{p}(\phi_i^{(2)}) \cdot \mathbf{n}^{(1)}, \mathbf{p}(\phi_j^{(1)}) \cdot \mathbf{n}^{(1)} \right\rangle_{0,\Gamma_c}. \quad (37c)$$

Moreover, the influence of γ on the system (36) has been eliminated using the triangle inequality in $L^2(\Gamma_c)$ and ensuring that $c_N > c$ such that one can use c_N instead of c in order to compute an estimation for the stabilization parameter, see Equation (21).

3.6. Discrete form of the transient problem

In what concerns the dynamical process of the mechanical system, it must be noted that $\mathbf{u}_h \in \mathcal{V}_h$ at each time instance $t \in \mathbb{T}$. This in turn means that the constants \hat{v}_i in (24a) are now time dependent, namely, $\hat{v}_i = \hat{v}_i(t)$ for all $t \in \mathbb{T}$. Projection of the inertial term in (7) onto $\mathcal{V}_h \times \mathcal{V}_h$ yields the mass matrix of the system. In this way, the complete semi-discretized form for the dynamical process of the mechanical system writes [44]

$$\mathbf{M}\ddot{\mathbf{u}}(t) + \mathbf{K}\hat{\mathbf{u}}(t) = \hat{\mathbf{F}} \quad \forall t \in \mathbb{T}, \quad (38)$$

where $\hat{\mathbf{u}}(t)$ denotes the semi-discretized DOFs, namely, the displacements, $\hat{\mathbf{u}}(t)$ denotes the DOFs related to the acceleration, $\hat{\mathbf{F}} = [\hat{\mathbf{F}}^{(1)} \quad \hat{\mathbf{F}}^{(2)}]^T$ denotes the system load vector, and \mathbf{M} denotes the system mass matrix, namely,

$$\mathbf{M} = \begin{bmatrix} \mathbf{M}^{(1)} & \mathbf{0} \\ \mathbf{0} & \mathbf{M}^{(2)} \end{bmatrix}. \quad (39)$$

The stiffness matrix \mathbf{K} in (38) is computed for each method as discussed before. Assuming periodicity of the solution with respect to the time, namely, $\hat{\mathbf{u}}(t) = \hat{\mathbf{u}} e^{i\omega t}$ for all $t \in \mathbb{T}$, Equation (38) yields the following generalized eigenvalue problem:

$$\mathbf{K}\hat{\mathbf{u}} = \omega^2 \mathbf{M}\hat{\mathbf{u}}, \quad (40)$$

which is to be solved for the natural eigenfrequencies ω_i of the system. The number of the resulting eigenfrequencies ω_i is equal to the number of the DOFs, meaning that $i = 1, \dots, 2n$. It should be, however, noted that the mass matrix must be extended with a zero block for the Lagrange multiplier methods, representing the zero inertial contributions of the Lagrange multiplier field into the system. Solution of the eigenvalue problem (40) results into undefined eigenfrequencies in the latter case. Those are related to the Lagrange multiplier DOFs [45] and thus do not need to be considered for the dynamical response of the system.

4. NUMERICAL RESULTS

In this section, two types of problems are used to compare the domain decomposition algorithms: steady-state elasticity problems for which closed form solutions exist and transient elasticity problems for which the reference solution in terms of eigenfrequencies has taken the solution of the same problem modeled with a single patch, a high discretization level, and a high polynomial degree. The material properties for all problems are set to be the same, that is, Young's modulus $E = 10^5$, Poisson ratio $\nu = 0.0$, and material density $\rho = 7810$. The thickness of the plate is chosen to be $h = 1$ for all the investigated problems. Moreover, the displacement and the force resultant fields u^α and $p^{\alpha\beta}$ with $\alpha, \beta = 1, 2$, respectively, are referring to the Cartesian basis throughout all the numerical investigations. Whenever the displacement or the force resultant field

is referring to a curvilinear basis, a subscript θ is used. Furthermore, the polynomial degrees of the NURBS basis functions with respect to the parametric coordinates ξ and η are denoted as r and q , respectively. Additionally, for all numerical examples, the penalty parameters are chosen as $\overline{\alpha} = E \times 10^3$ and $\overline{\alpha} = E$ for the penalty and the augmented Lagrange multiplier algorithms, respectively.

For the convergence study of the steady-state problems, the relative error is computed with the aid of the L^2 and H^1 norms. Those are defined over an open set Ω as follows:

$$\|\mathbf{v}\|_{L^2(\Omega)} = \|\mathbf{v}\|_{0,\Omega} = \left(\int_{\Omega} \mathbf{v} \cdot \mathbf{v} d\Omega \right)^{\frac{1}{2}} \quad \forall \mathbf{v} \in (L^2(\Omega))^2, \quad (41a)$$

$$\|\mathbf{v}\|_{H^1(\Omega)} = \|\mathbf{v}\|_{1,\Omega} = \left(\int_{\Omega} \mathbf{v} \cdot \mathbf{v} d\Omega + \int_{\Omega} \nabla \mathbf{v} : \nabla \mathbf{v} d\Omega \right)^{\frac{1}{2}} \quad \forall \mathbf{v} \in (H^1(\Omega))^2, \quad (41b)$$

where $L^2(\Omega)$ is the space of all square integrable functions in Ω , and $H^1(\Omega)$ is the space of all square integrable functions with square integrable derivatives in Ω , see [46] for more details. On the contrary, the relative error in the absolute value of the eigenfrequencies is computed for the transient problems, because this is of primary interest in the latter case.

4.1. Quarter of an annulus subject to uniform internal pressure

In this section, the numerical results using the DDMs are compared against the analytical ones for an annulus plate subject to uniform internal pressure. The structure is fully characterized by its inner and outer radius. For this problem, the inner and the outer radius are set to be $R_{\min} = 4$ and $R_{\max} = 5$, respectively. The magnitude of the pressure loading is set to be $p = 10^4$. Additionally, the annulus is modeled by its one quarter by applying symmetry boundary conditions that are roller supports in this case, see Figure 2(a). Analytical solution in terms of displacements and in terms of resultant forces exists [42], namely,

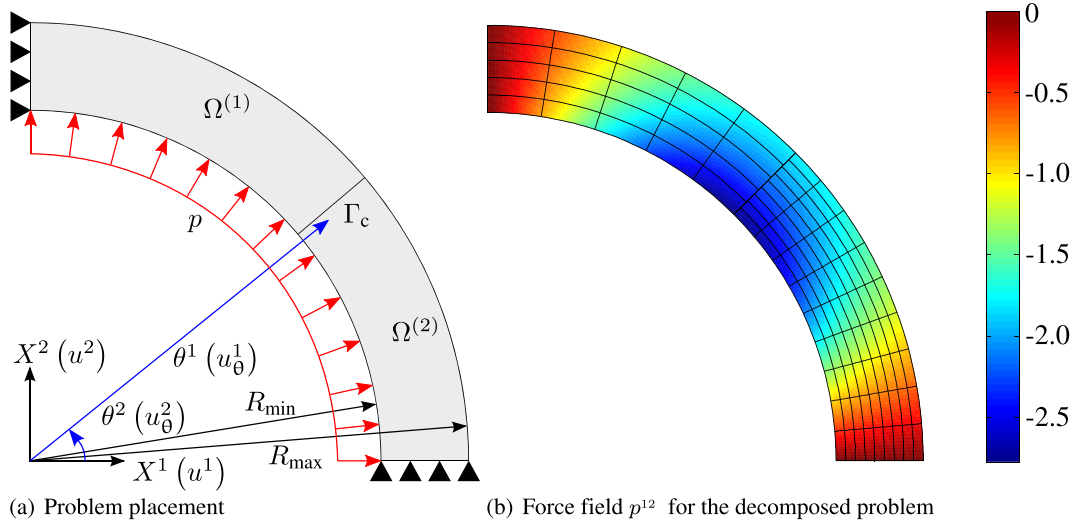


Figure 2. Quarter of an annulus subject to uniform internal pressure: postprocessing. Patch 1 is modeled with 25 elements and polynomial degrees $r_1 = 3$, $q_1 = 2$, and patch 2 is modeled with 81 elements and polynomial degrees $r_2 = 2$, $q_2 = 1$. (a) Problem placement and (b) force field p^{12} for the decomposed problem.

$$u_\theta^1(\theta^1, \theta^2) = \frac{p(1+\nu)}{Eh} \frac{R_{\min}^2}{(R_{\max}^2 - R_{\min}^2)} \left(\frac{1-2\nu}{1+\nu} \theta^1 + \frac{R_{\max}^2}{\theta^1} \right), \quad (42a)$$

$$p_\theta^{11}(\theta^1, \theta^2) = p \frac{R_{\min}^2}{R_{\max}^2 - R_{\min}^2} \left(1 - \left(\frac{R_{\max}}{\theta^1} \right)^2 \right), \quad (42b)$$

$$p_\theta^{22}(\theta^1, \theta^2) = p \frac{R_{\min}^2}{R_{\max}^2 - R_{\min}^2} \left(1 + \left(\frac{R_{\max}}{\theta^1} \right)^2 \right), \quad (42c)$$

for all $\theta^1 \in [R_{\min}, R_{\max}]$ and for all $\theta^2 \in [0, \frac{\pi}{2}]$. For this problem, the circumferential displacement component u_θ^2 and the shear force component p_θ^{12} are identically zero. In this case, the Cartesian and the curvilinear coordinate systems, X^1 - X^2 and θ^1 - θ^2 respectively, are related as follows:

$$X^1 = \theta^1 \cos \theta^2, \quad (43a)$$

$$X^2 = \theta^1 \sin \theta^2. \quad (43b)$$

The respective tensorial transformations from the curvilinear to the Cartesian basis write

$$u^1(\theta^1, \theta^2) = u_\theta^1(\theta^1, \theta^2) \cos \theta^2 - u_\theta^2(\theta^1, \theta^2) \theta^1 \sin \theta^2, \quad (44a)$$

$$u^2(\theta^1, \theta^2) = u_\theta^1(\theta^1, \theta^2) \sin \theta^2 + u_\theta^2(\theta^1, \theta^2) \theta^1 \cos \theta^2, \quad (44b)$$

$$p^{11}(\theta^1, \theta^2) = p_\theta^{11}(\theta^1, \theta^2) \cos^2 \theta^2 + p_\theta^{22}(\theta^1, \theta^2) \sin^2 \theta^2 - 2p_\theta^{12}(\theta^1, \theta^2) \sin \theta^2 \cos \theta^2, \quad (44c)$$

$$p^{22}(\theta^1, \theta^2) = p_\theta^{11}(\theta^1, \theta^2) \sin^2 \theta^2 + p_\theta^{22}(\theta^1, \theta^2) \cos^2 \theta^2 + 2p_\theta^{12}(\theta^1, \theta^2) \sin \theta^2 \cos \theta^2, \quad (44d)$$

$$p^{12}(\theta^1, \theta^2) = (p_\theta^{11}(\theta^1, \theta^2) - p_\theta^{22}(\theta^1, \theta^2)) \sin \theta^2 \cos \theta^2 + p_\theta^{12}(\theta^1, \theta^2) \cos 2\theta^2, \quad (44e)$$

for all $(\theta^1, \theta^2) \in [R_{\min}, R_{\max}] \times [0, \frac{\pi}{2}]$.

To initiate the discussion of the DDMs, as introduced in Section 2, the problem is divided into two subdomains. The interface is a straight line and placed such that it divides the annulus into two equal parts, see Figure 2(a). The shear resultant force field p^{12} is then visualized for a fixed pair of meshes illuminating the high interface compatibility of the solution. For this problem, no visualization of the deformed geometry is given, because this loading case results into uniform constant radial expansion of the plate. For the subsequent convergence study, patch 1 and patch 2 are systematically refined with $n_1 = (2i+1)^2$ and $n_2 = i^2$ elements respectively, where $i = 1, \dots, 25$ indicates the refinement level, see Figure 3. This refinement pattern is followed for the numerical investigations in Sections 4.1, 4.2, and 4.3.

Convergence of the displacements in the $H^1(\Omega)$ -norm can be found in Figure 4 for both low and high polynomial degrees. The penalty algorithm demonstrates the worst convergence for a fixed penalty parameter. It is also evident that the leveling off point for the penalty method is in the range of 10^{-5} , concerning the relative error in the domain displacements. The other methods perform similarly accurately, which is evident by the fact that their respective error graphs in the set of Figure 4 almost overlap. It should be noted that the Lagrange multiplier methods demonstrate rank deficiency for their respective system matrices, which is even more prominent the higher the polynomial degrees are chosen for the finite dimensional spaces (23a) and (23b), see the saddle point formulations (13) and (14) for the Lagrange multiplier and the augmented Lagrange multiplier formulations, respectively.

Concerning the force component p^{11} , convergence in the $L^2(\Omega)$ -norm is shown in Figure 5. As in the case of the displacements, for high polynomial degrees convergence is shown to be much faster than for low polynomial degrees. The leveling off point for the penalty algorithm has been detected in the range of 10^{-6} for the force component p^{11} , see Figure 5(b). Nevertheless, the rest of the methods perform equally good for the approximation of the force component p^{11} as for the displacements. The satisfaction level of the interface Neumann condition (5g) in the $L^2(\Gamma_c)$ -norm has also been investigated, see set of Figure 6. As before, both low and high polynomial degrees have been chosen for the comparison of the DDMs.

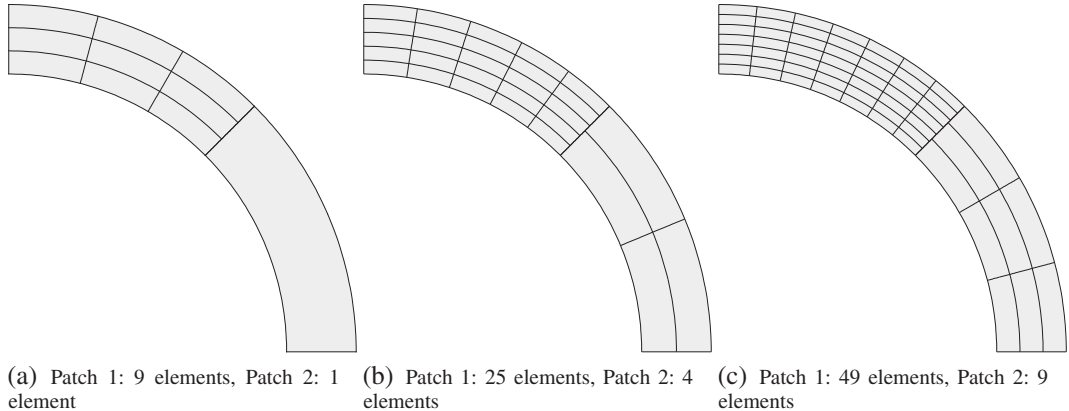


Figure 3. Quarter of an annulus subject to uniform internal pressure: systematic h-refinement (knot insertion) used for the convergence study starting from the coarsest mesh. (a) Patch 1: nine elements, patch 2: one element; (b) patch 1: 25 elements, patch 2: four elements; (c) patch 1: 49 elements, patch 2: nine elements.

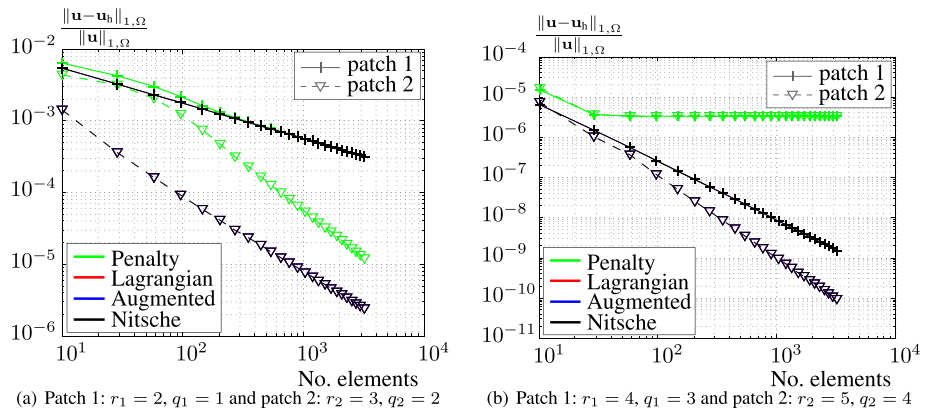


Figure 4. Quarter of an annulus subject to uniform internal pressure: convergence of the displacements in the $H^1(\Omega)$ -norm. (a) Patch 1: $r_1 = 2, q_1 = 1$ and patch 2: $r_2 = 3, q_2 = 2$ and (b) patch 1: $r_1 = 4, q_1 = 3$ and patch 2: $r_2 = 5, q_2 = 4$.

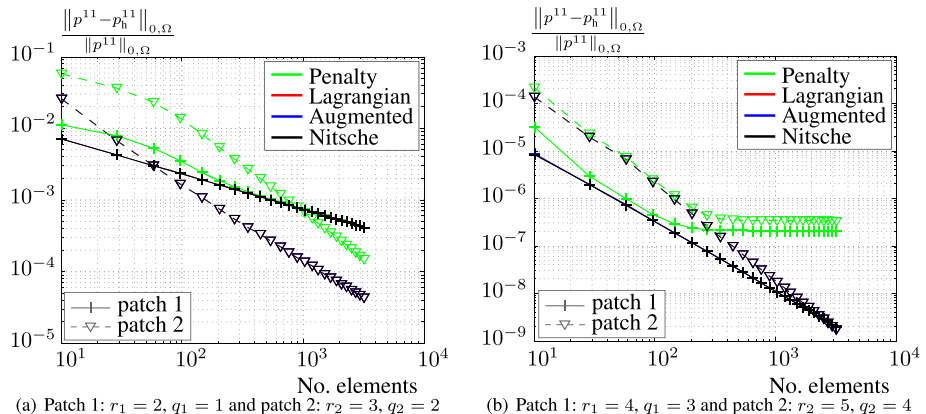


Figure 5. Quarter of an annulus subject to uniform internal pressure: convergence of the force component p^{11} in the $L^2(\Omega)$ -norm. (a) Patch 1: $r_1 = 2, q_1 = 1$ and patch 2: $r_2 = 3, q_2 = 2$ and (b) patch 1: $r_1 = 4, q_1 = 3$ and patch 2: $r_2 = 5, q_2 = 4$.

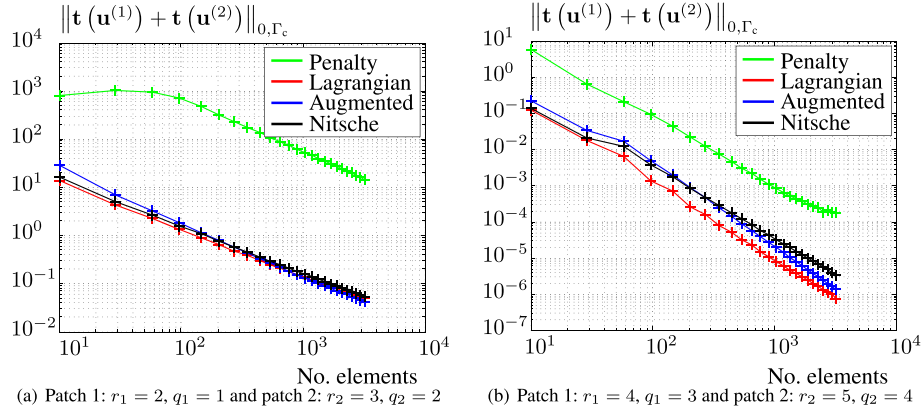


Figure 6. Quarter of an annulus subject to uniform internal pressure: convergence of the Neumann interface compatibility constraint in the $L^2(\Gamma_c)$ -norm. (a) Patch 1: $r_1 = 2, q_1 = 1$ and patch 2: $r_2 = 3, q_2 = 2$ and (b) patch 1: $r_1 = 4, q_1 = 3$ and patch 2: $r_2 = 5, q_2 = 4$.

4.2. Quarter of an annulus subject to tip shear load

Here, a quarter of an annulus subject to tip shear load is investigated. The plate is fixed opposite to its loaded edge, see Figure 7. Its geometric characteristics are the same as for the example of Section 4.1, but the shear loading is set here to be of magnitude $p = 10$. Analytical solution in terms of the resultant forces exists for this problem [47]:

$$p_{\theta}^{11}(\theta^1, \theta^2) = p \frac{1}{N_0} \sin \theta^2 \left(\theta^1 + \frac{R_{\min}^2 R_{\max}^2}{(\theta^1)^3} - \frac{R_{\min}^2 + R_{\max}^2}{\theta^1} \right), \quad (45a)$$

$$p_{\theta}^{22}(\theta^1, \theta^2) = p \frac{1}{N_0} \sin \theta^2 \left(3\theta^1 - \frac{R_{\min}^2 R_{\max}^2}{(\theta^1)^3} - \frac{R_{\min}^2 + R_{\max}^2}{\theta^1} \right), \quad (45b)$$

$$p_{\theta}^{12}(\theta^1, \theta^2) = -p \frac{1}{N_0} \cos \theta^2 \left(\theta^1 + \frac{R_{\min}^2 R_{\max}^2}{(\theta^1)^3} - \frac{R_{\min}^2 + R_{\max}^2}{\theta^1} \right), \quad (45c)$$

for all $\theta^1 \in [R_{\min}, R_{\max}]$ and for all $\theta^2 \in [0, \frac{\pi}{2}]$. The geometrical constant N_0 appearing in Equations (45a)–(45c) is defined as

$$N_0 = R_{\min}^2 - R_{\max}^2 + (R_{\min}^2 + R_{\max}^2) \ln \frac{R_{\max}}{R_{\min}}. \quad (46)$$

The coordinate transformation rules are the same as in Section 4.1, see Equations (43a)–(43b). Moreover, the tensorial transformation rules to the Cartesian coordinate system can be found in Equations (44c)–(44e). The additional feature of this problem is the curved interface. The distribution of the force component p^{22} along the plate is also visualized in Figure 8(b), whereas the scaled by 100 deformation is visualized in Figure 8(a) for a fixed pair of meshes in the two subdomains. In this case, the integration over Γ_c is no longer exact because of the fact that the Jacobian of the transformation from the physical space to the integration domain is no longer constant. However, it has been observed that the solution is accurately represented and that all the algorithms can handle curved interfaces without significant additional effort in terms of the numerical quadrature. Additionally, the interface Γ_c can be modeled exactly using both patches, that is, without gaps or overlaps, in the NURBS based IGA.

At first, the performance of the algorithms is compared with respect to their accuracy on the interface traction forces $\mathbf{t} = \mathbf{p} \cdot \mathbf{n}$. High convergence rates are observed for both low and high polynomial degrees, see Figure 9. However, the convergence rates are even higher for increasing polynomial degrees, see Figure 9(b). The leveling off point for the penalty method has been detected in the range of 10^{-5} in what concerns the relative error in the $L^2(\Omega)$ -norm for the interface traction forces. In addition, the Nitsche algorithm has the best accuracy in the coarse range of the respective meshes. However, for fine meshes, the error between all algorithms, except from the penalty one, is almost

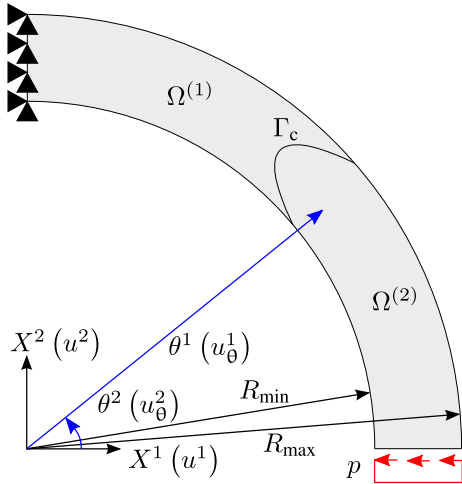


Figure 7. Quarter of an annulus subject to tip shear force: problem placement.

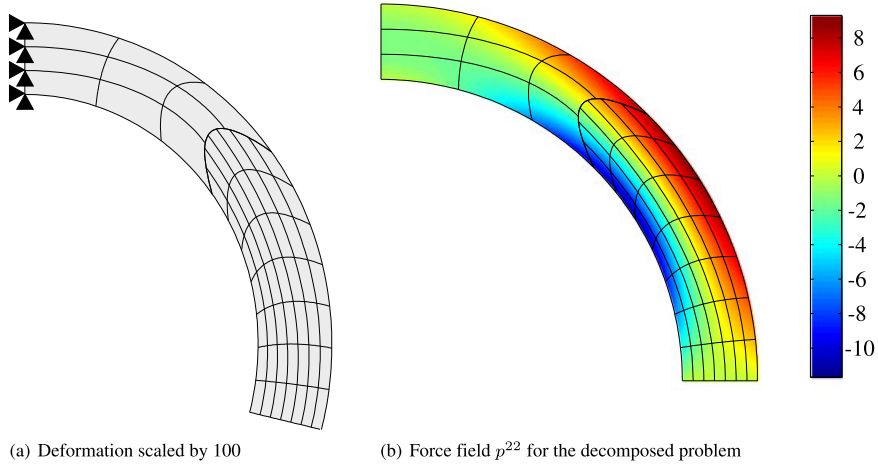


Figure 8. Quarter of an annulus subject to tip shear force: postprocessing. Patch 1 has been modeled with nine elements and polynomial degrees $r_1 = 4, q_1 = 3$, and patch 2 has been modeled with 49 elements and polynomial degrees $r_2 = 3, q_2 = 2$. (a) Deformation scaled by 100 and (b) force field p^{22} for the decomposed problem.

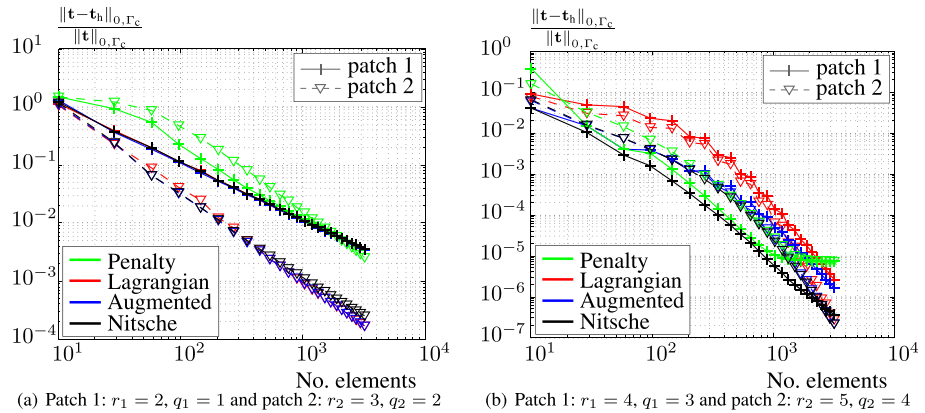


Figure 9. Quarter of an annulus subject to tip shear load: convergence of the interface traction forces in the $L^2(\Gamma_c)$ -norm. (a) Patch 1: $r_1 = 2, q_1 = 1$ and patch 2: $r_2 = 3, q_2 = 2$ and (b) patch 1: $r_1 = 4, q_1 = 3$ and patch 2: $r_2 = 5, q_2 = 4$.

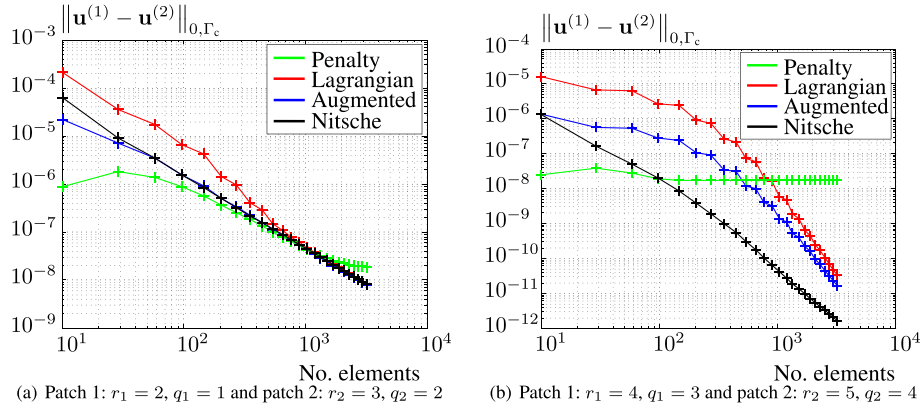


Figure 10. Quarter of an annulus subject to tip shear load: convergence of the interface Dirichlet condition in the $L^2(\Gamma_c)$ -norm. (a) Patch 1: $r_1 = 2, q_1 = 1$ and patch 2: $r_2 = 3, q_2 = 2$ and (b) patch 1: $r_1 = 4, q_1 = 3$ and patch 2: $r_2 = 5, q_2 = 4$.

the same. Then, the interface Dirichlet condition (5f) is tested, see Figure 10. The convergence rates for increasing polynomial degrees are higher as expected, see Figure 10(b). The leveling off point for the penalty method is observed in the range of 10^{-7} in the $L^2(\Gamma_c)$ -norm of the Dirichlet interface condition. The Nitsche algorithm is evidently the best performing one in terms of convergence and accuracy. It should be noted that the estimated stabilization parameter for the Nitsche algorithm is computed at each refinement level by solving the generalized eigenvalue problem using the inequality (21). It has been observed that the minimum eigenvalue of the Nitsche system converges to zero asymptotically. This verifies the observation that the largest eigenvalue of the generalized eigenvalue problem is an approximation for the constant $c > 0$ of the inequality (21) in the continuous setting. The finer the mesh, the better the approximation of c . An additional observation is that the stabilization parameter does not grow exponentially large with the number of the DOFs but remains orders of magnitude smaller than the penalty parameter needed to achieve the same order of accuracy. This is critical because in the case that the stabilization parameter is chosen much larger than necessary, the penalty-like term of the formulation (20) would dominate the discrete problem (35). The latter case would destroy the positive features of the Nitsche-type formulation, for example, the conditioning of the discrete equation system, leading essentially to the same results as in the penalty method.

In what concerns the choice of the convex combination parameter γ , Equation (15) can be seen as follows:

$$\bar{\mathbf{p}} = (1 - \gamma)\mathbf{p}^{(1)} + \gamma\mathbf{p}^{(2)}, \quad (47)$$

by restricting the first argument of $\bar{\mathbf{p}}$ into subdomain $\Omega^{(1)}$ and its second argument into subdomain $\Omega^{(2)}$. It has been noted that the Nitsche parameter γ has an influence on the side where the error is shifted, see set of Figure 11. Thus, by choosing $\gamma = 0$, meaning that $\bar{\mathbf{p}} = \mathbf{p}^{(1)}$, the error is shifted towards the subdomain $\Omega^{(2)}$. Consequently, a choice of $\gamma = 1$ would imply $\bar{\mathbf{p}} = \mathbf{p}^{(2)}$, which has the implication the error to be shifted towards the subdomain $\Omega^{(1)}$. Even though the differences are not significant from one extreme to the other, the choice $\gamma = \frac{1}{2}$ serves for the fair distribution of the error among the subdomains. Thus, for all the numerical examples, $\gamma = \frac{1}{2}$ has been chosen for the free parameter of the Nitsche method.

4.3. Infinite elastic plate with circular hole in tension regime

In this section, the performance of the DDMs is investigated on the problem of an infinite elastic plate with circular hole, which is subject to tension loading in $X^1 = -\infty$ and $X^1 = \infty$. The plate is modeled using its one quarter by applying the symmetry boundary conditions, roller supports, as well as the exact tractions at its upper and right edges, see Figure 12. Analytical solution in terms of the displacements in the Cartesian basis can be obtained via analytical methods as explained in [47]:

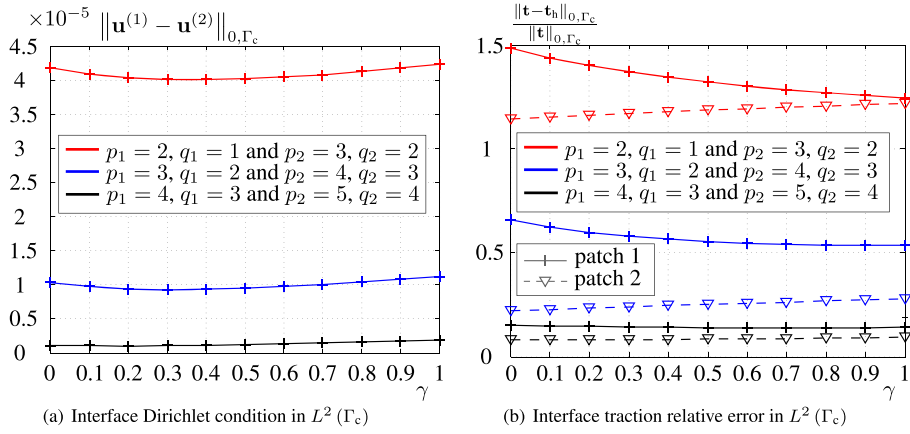


Figure 11. Quarter of an annulus subject to tip shear load: influence of the convex linear combination parameter $\tilde{\gamma}$ on the solution in the Nitsche approach. Patch 1 has been discretized using one element, and patch 2 has been discretized using nine elements. (a) Interface Dirichlet condition in $L^2(\Gamma_c)$ and (b) Interface traction relative error in $L^2(\Gamma_c)$.

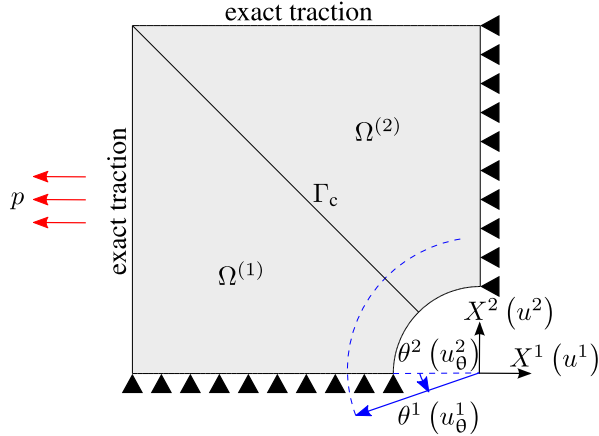


Figure 12. Infinite plate with circular hole: problem placement.

$$u^1(\theta^1, \theta^2) = -\frac{pR}{8\mu h} \left(\frac{\kappa+1}{R} \theta^1 \cos \theta^2 + 2R \frac{(1+\kappa) \cos \theta^2 + \cos 3\theta^2}{\theta^1} - 2R^3 \frac{\cos 3\theta^2}{(\theta^1)^3} \right), \quad (48a)$$

$$u^2(\theta^1, \theta^2) = -\frac{pR}{8\mu h} \left(\frac{\kappa-3}{R} \theta^1 \sin \theta^2 + 2R \frac{(1-\kappa) \sin \theta^2 + \sin 3\theta^2}{\theta^1} - 2R^3 \frac{\sin 3\theta^2}{(\theta^1)^3} \right). \quad (48b)$$

using for the resultant forces in the curvilinear basis, that is, [47]:

$$p_\theta^{11}(\theta^1, \theta^2) = \frac{1}{2} p \left(1 - \left(\frac{R}{\theta^1} \right)^2 \right) + \frac{1}{2} p \cos 2\theta^2 \left(1 - 4 \left(\frac{R}{\theta^1} \right)^2 + 3 \left(\frac{R}{\theta^1} \right)^4 \right), \quad (49a)$$

$$p_\theta^{22}(\theta^1, \theta^2) = \frac{1}{2} p \left(1 + \left(\frac{R}{\theta^1} \right)^2 \right) - \frac{1}{2} p \cos 2\theta^2 \left(1 + 3 \left(\frac{R}{\theta^1} \right)^4 \right), \quad (49b)$$

$$p_\theta^{12}(\theta^1, \theta^2) = -\frac{1}{2} p \sin 2\theta^2 \left(1 + 2 \left(\frac{R}{\theta^1} \right)^2 - 3 \left(\frac{R}{\theta^1} \right)^4 \right), \quad (49c)$$

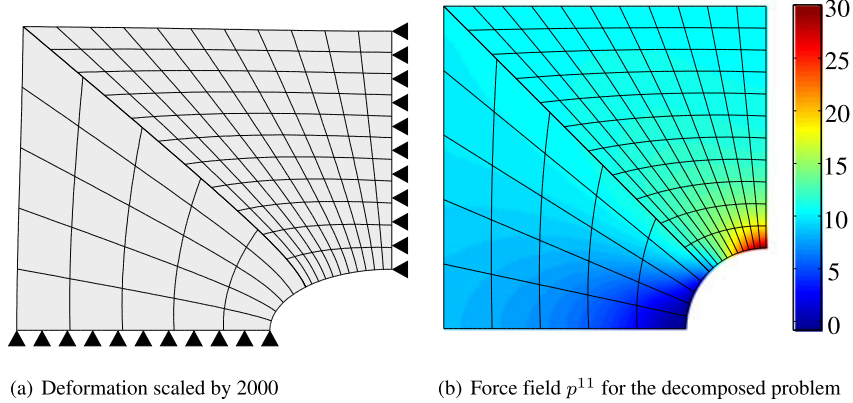


Figure 13. Infinite plate with circular hole: postprocessing. Patch 1 has been modeled with 25 elements and polynomial degrees $r_1 = 4, q_1 = 5$, and patch 2 has been modeled with 121 elements and polynomial degrees $r_2 = 3, q_2 = 2$. (a) Deformation scaled by 2000 and (b) force field p^{11} for the decomposed problem.

for all $(\theta^1, \theta^2) \in \overline{\Omega}_\theta$, where Ω_θ denotes the image of the domain Ω under the inverse of the coordinate mapping:

$$X^1 = -\theta^1 \cos \theta^2, \quad (50a)$$

$$X^2 = \theta^1 \sin \theta^2, \quad (50b)$$

and the analogous to Equations (44a)–(44b) transformation rules for this case. The constants μ and κ used in Equations (48a) and (48b) are defined as

$$\mu = \frac{E}{2(1+\nu)}, \quad (51a)$$

$$\kappa = \frac{3-\nu}{1+\nu}. \quad (51b)$$

The tensorial transformations of the force resultants to the Cartesian basis, defined in Equations (44c)–(44e), remain unaltered in this case too. The rectangular plate has length size equal to $L = 4$ and radius of its hole equal to $R = 1$. The tensional loading is chosen to be of magnitude $p = 10$ for this example also. The scaled by 2000 deformation and the distribution of the force component p^{11} along the plate are then visualized in Figures 13(a) and 13(b) respectively, emphasizing the smoothness of the results for high NURBS polynomial degrees.

Additionally, a comparison of C^0 -continuous basis functions to basis functions that attain high inter-element continuity is performed. For this reason, patch 1 is discretized with 16 elements and polynomial degree $r_1 = 4$ along the interface, that is, the basis functions are C^3 -continuous between the elements. Subsequently, patch 2 is discretized with 121 elements which have polynomial degree $q_2 = 1$ along the interface, i.e. the basis functions are C^0 -continuous, which in turn means that the approximated force resultants are discontinuous between the elements. It is evident that the C^3 -continuous basis functions can approximate sufficiently the exact solution even with few elements, whereas the low order ones demonstrate oscillations, attributed to the discontinuous derivatives of the basis functions, see Figure 14. This comparison demonstrates also the superiority of IGA to classical finite element analysis.

Next, the convergence of the interface displacements in the $H^1(\Gamma_c)$ -norm and tractions in the $L^2(\Gamma_c)$ -norm is investigated, see set of Figures 15 and 16, respectively. As expected, the penalty method for a fixed penalty parameter demonstrates the worst rates of convergence for both displacements and tractions. The rest of the methods perform equally accurately. It is important to note that the Nitsche method always yields a positive definite system matrix, in contrast to the Lagrange multiplier methods, which is in addition, well conditioned. Finally, the Dirichlet and the Neumann interface conditions are investigated in the $L^2(\Gamma_c)$ -norm, see the set of Figures 17 and 18 respectively. The penalty method performs inaccurately especially in what concerns the Neumann interface

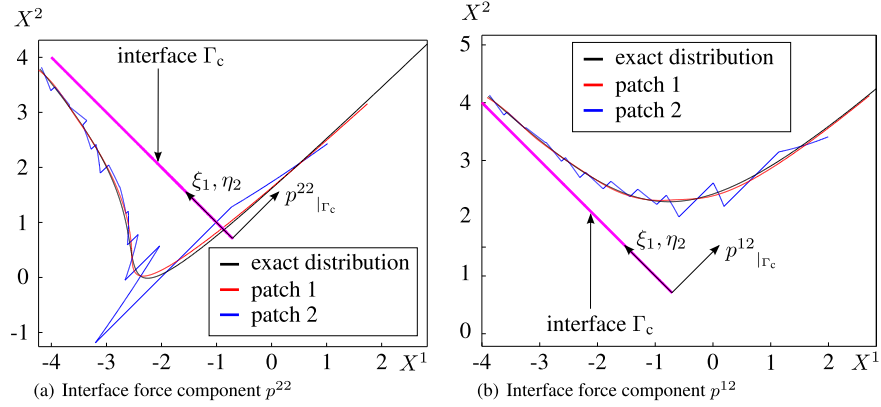


Figure 14. Infinite plate with circular hole: interface force distribution for both patches and the analytical solution: patch 1 has been modeled with 16 elements and polynomial degrees $r_1 = 4, q_1 = 3$, and patch 2 has been modeled with 121 elements and polynomial degrees $r_2 = 1, q_2 = 2$. (a) Interface force component p^{22} and (b) interface force component p^{12} .

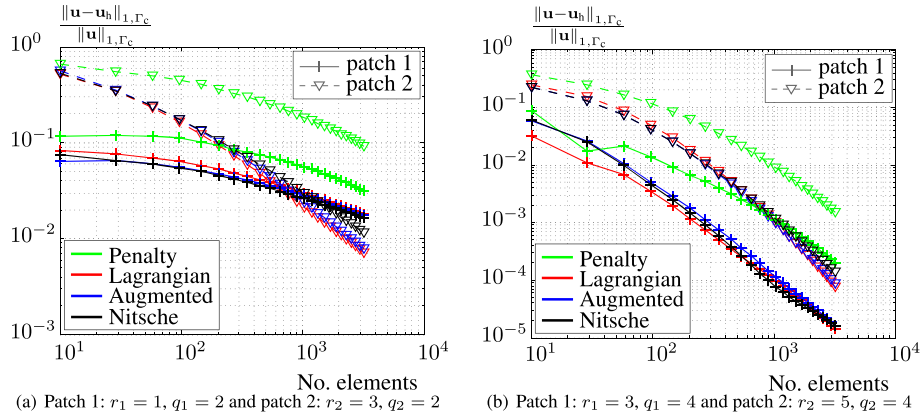


Figure 15. Infinite plate with circular hole: convergence of the displacements in the $H^1(\Gamma_c)$ -norm. (a) Patch 1: $r_1 = 1, q_1 = 2$ and patch 2: $r_2 = 3, q_2 = 2$ and (b) patch 1: $r_1 = 3, q_1 = 4$ and patch 2: $r_2 = 5, q_2 = 4$.

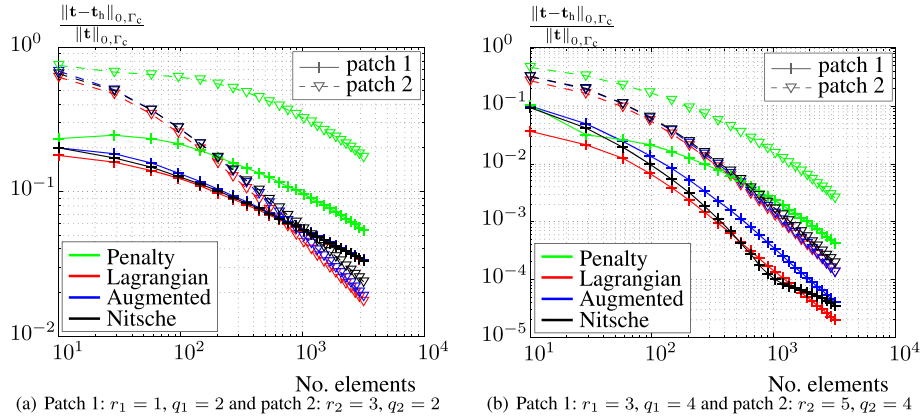


Figure 16. Infinite plate with circular hole: convergence of the interface tractions in the $L^2(\Gamma_c)$ -norm. (a) Patch 1: $r_1 = 1, q_1 = 2$ and patch 2: $r_2 = 3, q_2 = 2$ and (b) patch 1: $r_1 = 3, q_1 = 4$ and patch 2: $r_2 = 5, q_2 = 4$.

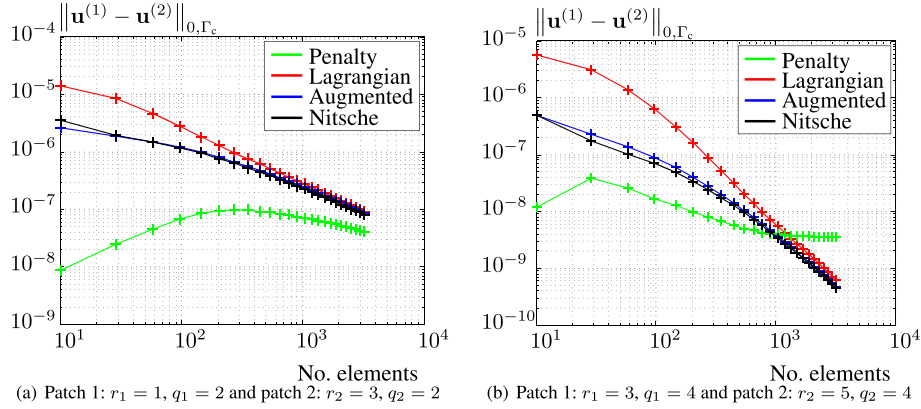


Figure 17. Infinite plate with circular hole: convergence of the Dirichlet interface condition in the $L^2(\Gamma_c)$ -norm. (a) Patch 1: $r_1 = 1, q_1 = 2$ and patch 2: $r_2 = 3, q_2 = 2$ and (b) patch 1: $r_1 = 3, q_1 = 4$ and patch 2: $r_2 = 5, q_2 = 4$.

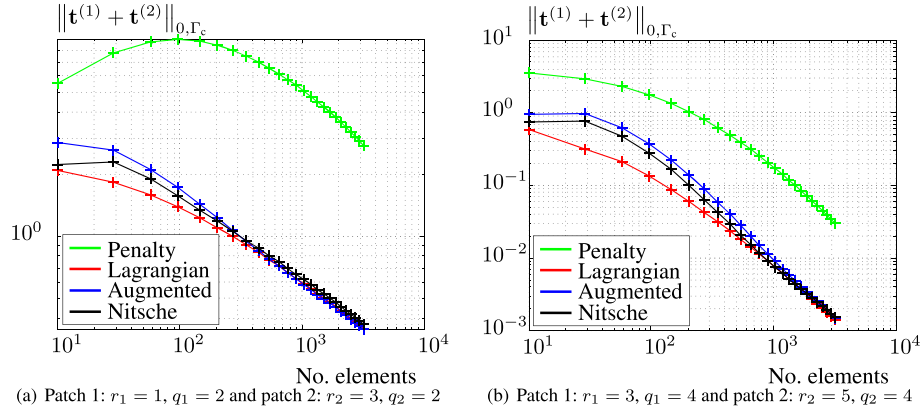


Figure 18. Infinite plate with circular hole: convergence of the Neumann interface condition in the $L^2(\Gamma_c)$ -norm. (a) Patch 1: $r_1 = 1, q_1 = 2$ and patch 2: $r_2 = 3, q_2 = 2$ and (b) patch 1: $r_1 = 3, q_1 = 4$ and patch 2: $r_2 = 5, q_2 = 4$.

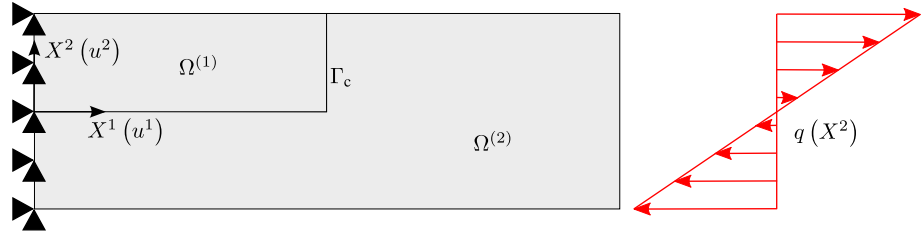


Figure 19. Rectangular elastic plate subject to in-plane bending moment: problem placement.

condition and for low polynomial degrees. On the contrary, high polynomial degrees seem to make the penalty algorithm to produce improved rates of convergence.

4.4. Rectangular elastic plate subject to in-plane bending moment with singularities in the parametrization

The last steady-state problem to be investigated is that of a rectangular elastic plate $\bar{\Omega}$, fixed at its one edge while subject to in-plane bending moment at its free edge, which is subdivided into two subdomains $\Omega^{(1)}$ and $\Omega^{(2)}$, see Figure 19. The goal of this study is to comparatively test the numerical behavior of the DDMs for cases with singularities in the parametrization. The subdomain $\Omega^{(1)}$ is chosen to be rectangular with length in X^1 -direction to be $L_1 = 3$ and height in X^2 -direction

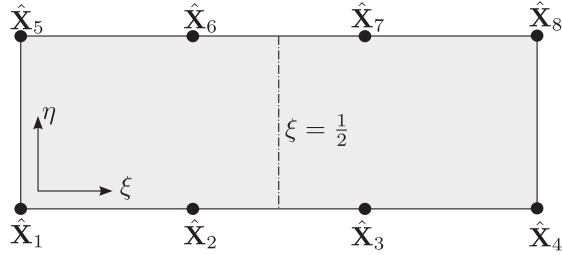


Figure 20. Rectangular elastic plate subject to in-plane bending moment: initial NURBS setting of the two patches before forming their final geometry.

to be $H_1 = 1$. On the other hand, subdomain $\Omega^{(2)}$ is chosen to be L-shaped with its minimum and maximum length in X^1 -direction being $L_1 = 3$ and $L_2 = 6$, respectively. Additionally, its minimum and maximum height in X^2 -direction has chosen to be $H_1 = 1$ and $H_2 = 2$, respectively. The distribution of the load at the free edge of patch 2 is linear:

$$q(X^2) = 2 \frac{q_0}{H} X^2 \quad \forall X^2 \in \left[-\frac{H}{2}, \frac{H}{2} \right]. \quad (52)$$

The maximum amplitude of the applied load is chosen to be $q_0 = 10^3$. For this example, there is a closed form solution via the Airy's stress function [48], which can be used to obtain a closed form expression for the resultant force and subsequently for the displacement field, which in the Cartesian basis writes

$$p^{11}(X^1, X^2) = 2 \frac{q_0}{H} X^2 \quad \forall (X^1, X^2) \in \overline{\Omega}, \quad (53a)$$

$$u^1(X^1, X^2) = 2 \frac{q_0}{EHh} X^1 X^2 \quad \forall (X^1, X^2) \in \overline{\Omega}, \quad (53b)$$

$$u^2(X^1, X^2) = -\frac{q_0}{EHh} (X^1)^2 \quad \forall (X^1, X^2) \in \overline{\Omega}, \quad (53c)$$

with p^{22} and p^{12} force components identically zero in $\overline{\Omega}$, because within our investigation $v = 0$. For this specific case, the variable H , which appear in Equations (52) and (53a)–(53c), is equal to $H_2 = 2$, that is, the length of patch 2 in the X^2 -direction. In this problem, the interface Γ_c is no longer a C^∞ -continuous curve, as in the previous problems, but a piecewise linear curve. The additional feature of this problem is that both subdomains are modeled as NURBS patches such that their individual parametrizations are singular over the interface Γ_c . For both patches, the following open knot vectors are used:

$$\Xi = [0 \ 0 \ 0 \ \frac{1}{2} \ 1 \ 1 \ 1], \quad (54a)$$

$$\mathcal{H} = [0 \ 0 \ 1 \ 1]. \quad (54b)$$

Moreover, the initial geometrical setting of both patches $\Omega^{(1)}$ and $\Omega^{(2)}$, together with the knot at $\xi = \frac{1}{2}$ and the control points \hat{X}_i , $i = 1, \dots, 8$, can be seen in Figure 20. In that case, the geometrical map $\mathbf{G} : \Xi \times \mathcal{H} \rightarrow \overline{\Omega}$, namely,

$$\mathbf{G} = \sum_{i=1}^8 R^{i,r,q} \hat{X}_i, \quad (55)$$

is regular in $\Xi \times \mathcal{H}$ and $R^{i,r,q} : \Xi \times \mathcal{H} \rightarrow \mathbb{R}$, $i = 1, \dots, 8$, denote the NURBS basis functions that attain polynomial degree $r = 2$ and $q = 1$ along ξ and η parametric lines, respectively. The latter means that the Jacobian

$$\mathbf{J} = \frac{d(X^1, X^2)}{d(\xi, \eta)} = \begin{pmatrix} \frac{\partial X^1}{\partial \xi} & \frac{\partial X^1}{\partial \eta} \\ \frac{\partial X^2}{\partial \xi} & \frac{\partial X^2}{\partial \eta} \end{pmatrix}, \quad (56)$$

has a strictly positive determinant at each parametric location.

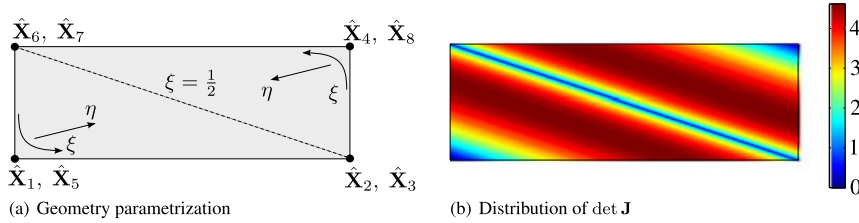


Figure 21. Rectangular elastic plate subject to in-plane bending moment: parametrization singularities for patch 1. (a) Geometry parametrization and (b) distribution of $\det \mathbf{J}$.

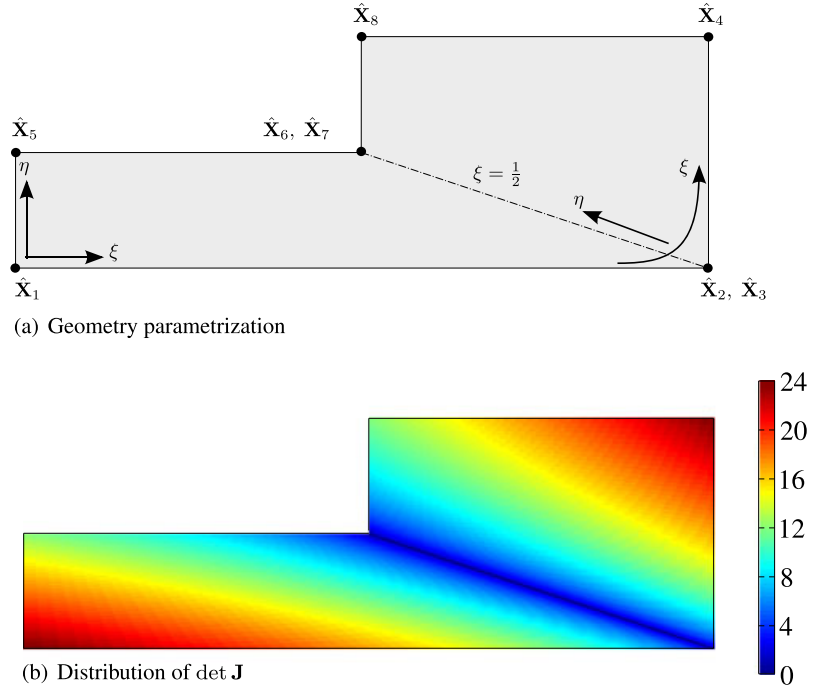


Figure 22. Rectangular elastic plate subject to in-plane bending moment: Parametrization singularities for patch 2. (a) Geometry parametrization (b) Distribution of $\det \mathbf{J}$.

Then, using the prototype geometry given in Figure 20, the control points are shifted as shown in Figures 21(a) and 22(a) such that the parametrization for each patch gets singular, meaning that $\det \mathbf{J} = 0$ at some parametric locations. Subsequently, the $\det \mathbf{J}$ over patch 1 and patch 2 is visualized in Figures 21(b) and 22(b), respectively, showing that there are three parametric locations along Γ_c in patch 1 and two parametric locations along Γ_c in patch 2 where the parametrization gets singular. The scaled by 10 deformed configuration of the plate and the corresponding p^{11} component of the resultant force field are visualized in Figures 23(a) and 23(b), respectively, for a fixed pair of meshes emphasizing the compatibility of the results even for highly distorted parametrizations. For the refinement studies, $r = 2$ and $q = 1$ are chosen as low polynomial degrees, whereas $r = 3$ and $q = 2$ are chosen as high polynomial degrees, for both patches. Additionally, both patches are refined uniformly in their parameter space with $n_1 = (2i + 3)^2$ and $n_2 = (2i + 1)^2$ elements for patch 1 and patch 2, respectively, where $i = 1, \dots, 20$ indicates the refinement level as in Section 4.1. The analytical solution for this problem is quadratic with respect to the displacements, see Equations (53b) and (53c). The numerical solution $\mathbf{u}_h \in \mathcal{V}_h$

$$\mathbf{u}_h = \tilde{\mathbf{u}}_h \circ \mathbf{G}^{-1} \quad \text{in } \Omega, \quad (57)$$

is not a polynomial in the Cartesian space because the geometrical map, defined in Equation (55), is in this case nonlinear. However, the displacement field in the NURBS parameter space $\tilde{\mathbf{u}}_h$:

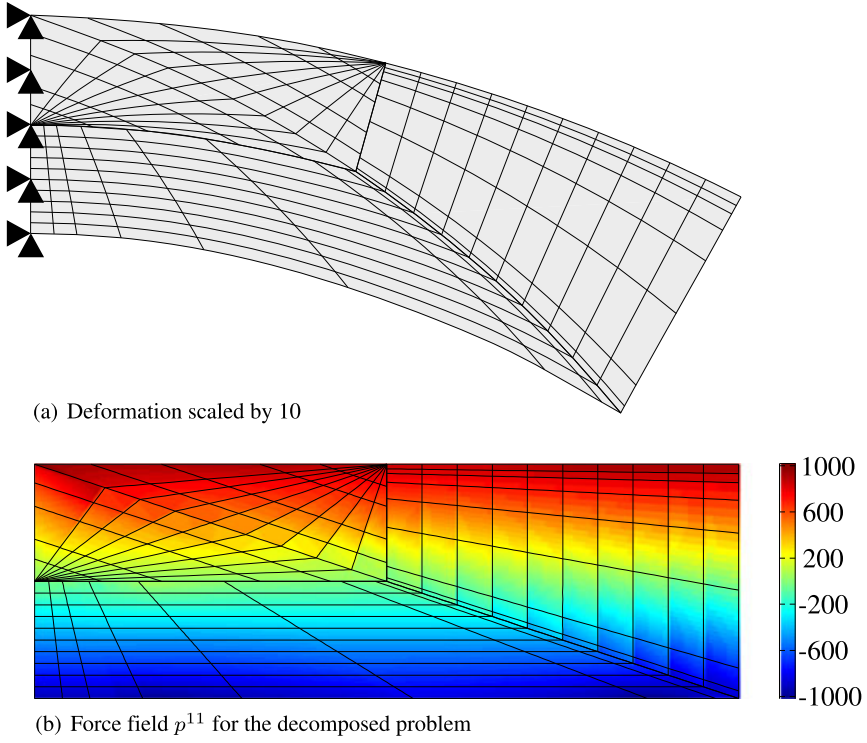


Figure 23. Rectangular elastic plate subject to in-plane bending moment: postprocessing. Patch 1 has been modeled with 49 elements and polynomial degrees $r_1 = 2, q_1 = 1$, and patch 2 has been modeled with 160 elements and polynomial degrees $r_2 = 2, q_2 = 1$. (a) Deformation scaled by 10 and (b) force field p^{11} for the decomposed problem.

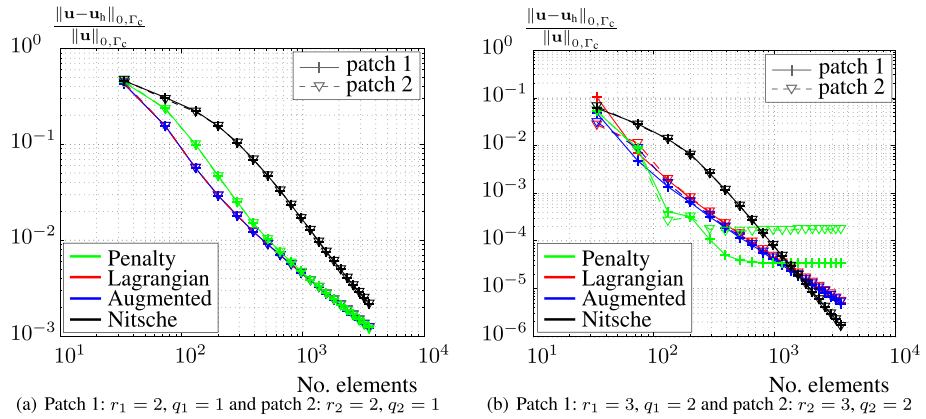


Figure 24. Rectangular elastic plate subject to in-plane bending moment: convergence of the displacements in the $L^2(\Gamma_c)$ -norm. (a) Patch 1: $r_1 = 2, q_1 = 1$ and patch 2: $r_2 = 2, q_2 = 1$ and (b) patch 1: $r_1 = 3, q_1 = 2$ and patch 2: $r_2 = 3, q_2 = 2$.

$\Xi \times \mathcal{H} \rightarrow \mathbb{R}^2$, is a piecewise polynomial because all control point weights are chosen to be equal to one. Therefore, it makes sense to perform a refinement study even for NURBS polynomial approximations of order higher than one. Subsequently, the performance of all the domain decomposition algorithms in the relative displacement error measured in the $L^2(\Gamma_c)$ -norm when uniformly refining the geometry resolution using knot insertion is investigated, see Figure 24. Then, it can be identified that all methods perform almost equally accurately for low polynomial degrees, see Figure 24(a). On the contrary, the superiority of the Lagrange multiplier methods and the

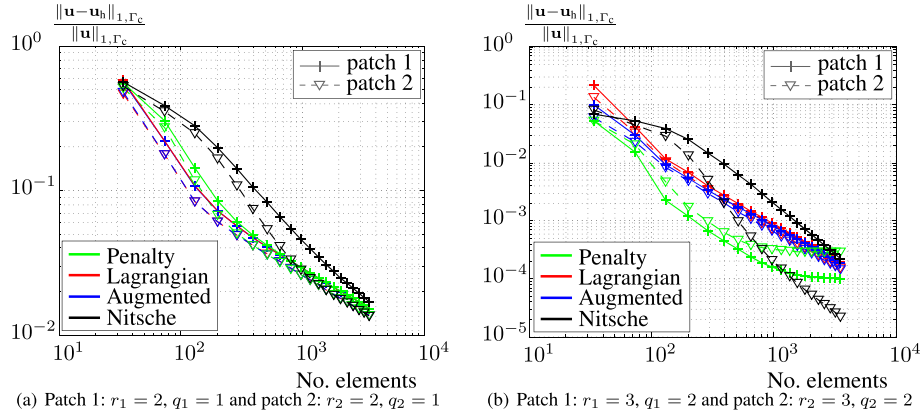


Figure 25. Rectangular elastic plate subject to in-plane bending moment: convergence of the displacements in the $H^1(\Gamma_c)$ -norm. (a) Patch 1: $r_1 = 2, q_1 = 1$ and patch 2: $r_2 = 2, q_2 = 1$ and (b) patch 1: $r_1 = 3, q_1 = 2$ and patch 2: $r_2 = 3, q_2 = 2$.

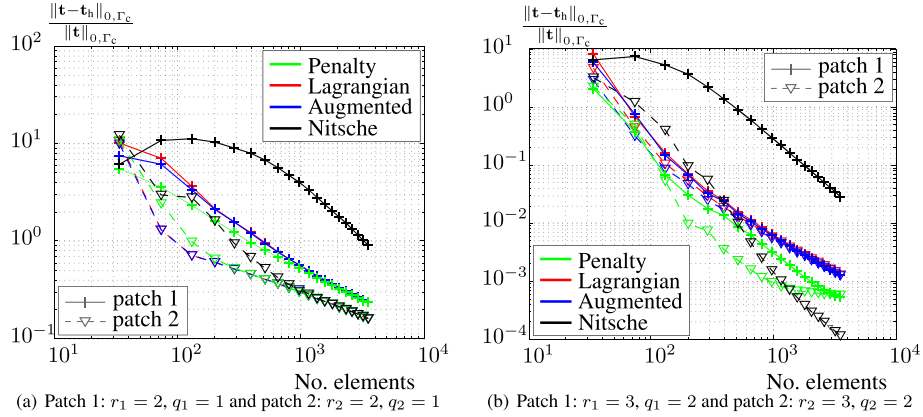


Figure 26. Rectangular elastic plate subject to in-plane bending moment: convergence of the tractions in the $L^2(\Gamma_c)$ -norm. (a) Patch 1: $r_1 = 2, q_1 = 1$ and patch 2: $r_2 = 2, q_2 = 1$ and (b) patch 1: $r_1 = 3, q_1 = 2$ and patch 2: $r_2 = 3, q_2 = 2$.

Nitsche-type method against the penalty one is evident for high polynomial degrees, see Figure 24(b). It should be noted that for the numerical investigation using a low order basis, see Figure 24(a), the leveling off point of the penalty method has not been reached even by using more than 3000 elements. That is because the maximum relative error succeeded at this case is in the range of 1%. For this investigation, the penalty method reaches its level off point at 0.01% of the relative displacement error in the $L^2(\Gamma_c)$ -norm. A similar study is performed, where the relative displacement error in the $H^1(\Gamma_c)$ -norm is measured, see Figure 25. The results for this convergence study preserve the same rates as in the case of the L^2 -norm but in a higher level of the relative error, which is expected because also derivatives of the displacement field are involved in this case.

As last, the relative traction error in the $L^2(\Gamma_c)$ -norm is tracked for each refinement level and depicted in Figure 26. In the case of low polynomial degrees, all algorithms produce a relative error in the order of 10% when using more than 3000 elements, see Figure 26(a). This behavior is corrected when using higher polynomial degrees where, with the same number of elements as before, the relative error reaches the level of 0.1–0.01%, see Figure 26(b).

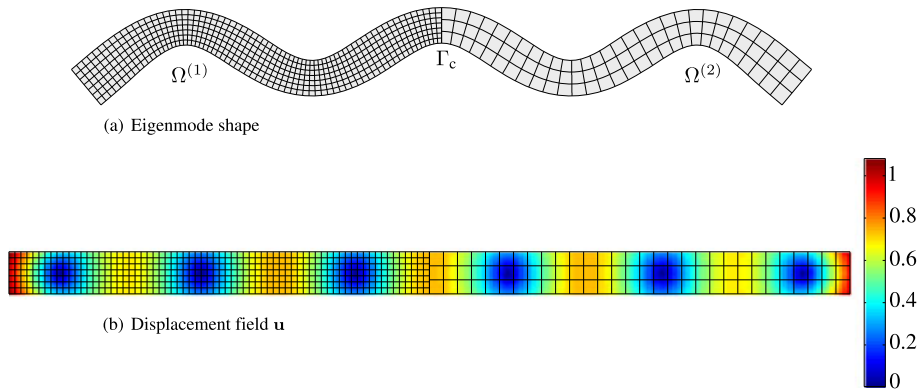


Figure 27. Rectangular plate: postprocessing. Visualization of the eigenmode shape corresponding to the eigenfrequency $\omega_9 = 7.0145 \times 10^{-1}$. Patch 1 has been modeled with 490 elements and polynomial degrees $r_1 = q_1 = 3$, and patch 2 has been modeled with 90 elements and polynomial degrees $r_2 = q_2 = 4$. (a) Eigenmode shape and (b) displacement field u .

It is overall concluded that the elaborated DDMs can handle parametrization singularities, even when those appear along the interface. This observation may form the basis for a further fundamental mathematical investigation on the analysis of multiple domains with singularities on the interface parametrization.

4.5. Eigenfrequency analysis and domain decomposition methods.

The next set of problems demonstrates the applicability of the aforementioned methods into structural dynamics. The eigenfrequencies and the eigenmode shapes making use of a consistent mass matrix within all the domain decomposition algorithms are computed. The corresponding eigenvectors are scaled such that their length is unit. Two examples are used: a rectangular and a circular plate. For the corresponding refinement studies, patch 1 and patch 2 are refined uniformly using $n_1 = i^2$ and $n_2 = (2i + 7)^2$ elements, respectively, where $i = 1, \dots, 20$ indicates the refinement level as in Section 4.1.

4.5.1. The rectangular plate. The eigenfrequencies and the eigenmode shapes of a free rectangular plate are investigated in this section. The size of the plate edge is $L_1 = 20$ and $L_2 = 1$ in X^1 -direction and X^2 -direction, respectively. The dimension of the rectangular plate in X^1 -direction is chosen much larger than its dimension in X^2 -direction such that to obtain results similar to the beam theory. For the reference solution, the same problem is solved using one patch, NURBS polynomial degrees $r = q = 15$, and 2000 elements of rectangular shape. Additionally, the ninth eigenmode shape, Figure 27(a), and the corresponding displacement field, Figure 27(b), are visualized, when sorting the eigenmode shapes in ascending order with respect to their corresponding eigenfrequencies excluding the rigid body modes, that is, the zero frequency modes.

In Figure 28, the convergence of the first eigenfrequency in the relative error for all the DDMs, for low and high polynomial degrees, can be seen. The leveling off point for the penalty method has been detected in the range of 10^{-5} while the rest of the methods demonstrate high convergence rates with the Nitsche algorithm to be the most stable one in general, see Figure 28(b). Convergence in the ninth eigenfrequency is shown in Figure 29. For this eigenfrequency, the leveling off point for the penalty approach has not been observed up to a relative error of 10^{-5} , and all the methods perform equally accurately. Equivalent results can also be obtained for the rest of the eigenfrequencies; however, the low frequency ones are shown here because those are the most prominent to be excited in a dynamical action of the mechanical system.

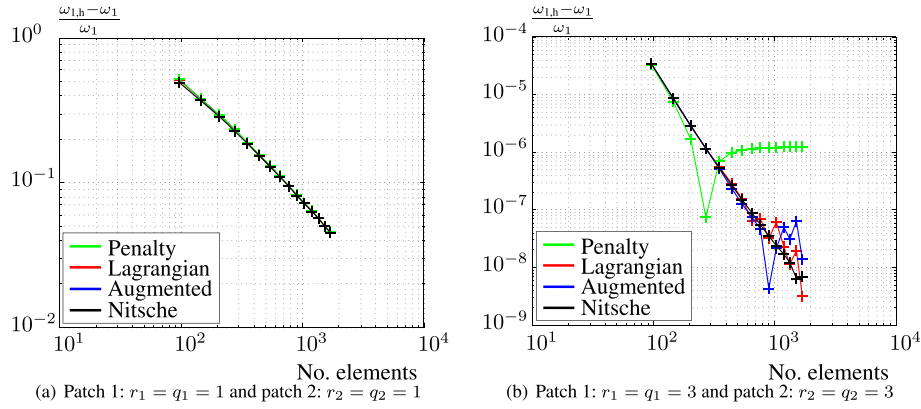


Figure 28. Rectangular plate: convergence of the 1st eigenfrequency in the relative error. (a) Patch 1: $r_1 = q_1 = 1$ and patch 2: $r_2 = q_2 = 1$ and (b) patch 1: $r_1 = q_1 = 3$ and patch 2: $r_2 = q_2 = 3$.

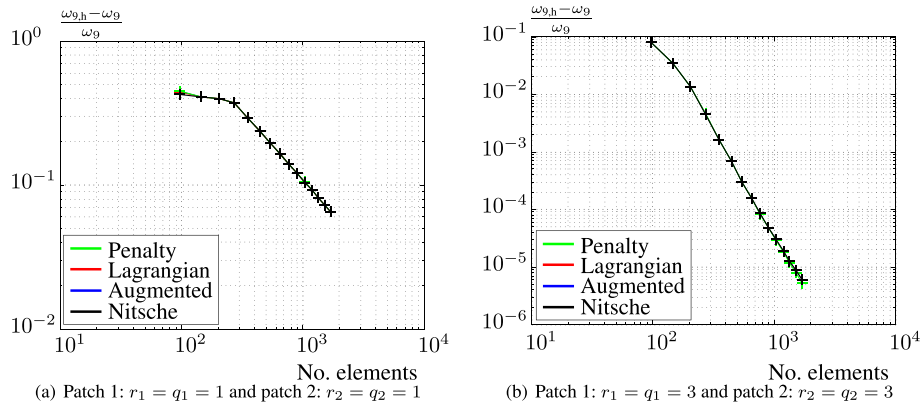


Figure 29. Rectangular plate: convergence of the 9th eigenfrequency in the relative error. (a) Patch 1: $r_1 = q_1 = 1$ and patch 2: $r_2 = q_2 = 1$ and (b) patch 1: $r_1 = q_1 = 3$ and patch 2: $r_2 = q_2 = 3$.

4.5.2. The circular plate. A circular plate modeled by its one quarter and by applying symmetry boundary conditions is numerically confronted in this section. As reference solution in this problem, a single patch model with 3600 elements and polynomial degrees $r = 17$ and $q = 16$ is used. The 60 elements adjacent to the middle of the circular plate \mathbf{x}_0 are degenerated into triangles, but this does not affect the analysis in the rest of the domain $\overline{\Omega} \setminus \{\mathbf{x}_0\}$. However, the resultant force field is undefined at \mathbf{x}_0 . Following the same sequence as in the steady-state numerical examples, the problem to be investigated is decomposed into two subdomains that share a curved interface, see Figure 30. The first eigenmode shape, Figure 31(a), and the corresponding displacement field, Figure 31(b), are then visualized, when sorting the eigenmode shapes with respect to the corresponding eigenfrequencies in an ascending order. This mode shape corresponds to the compression of the circular disk. Subsequently, the relative error in the first, the fifth, and the ninth eigenfrequency of the system are computed using the domain decomposition algorithms developed in Section 2. It is overall observed that all methods demonstrate high accuracy and robustness even for low discretization level and especially for high polynomial degrees. However, the penalty method demonstrates convergence up to a certain level of the relative error for a fixed penalty parameter. On the other hand, the Lagrange multiplier based methods may result into oscillatory results for a high discretization level and polynomial degree as in the steady-state cases. Convergence in the eigenfrequency $\omega_1 = 1.1822$ is shown in Figure 32. For low polynomial degrees and high discretization level, it seems that the penalty method performs better than the rest of the methods, see Figure 32(a). However, for high polynomial degrees, the leveling off point of the penalty method is detected in the range of

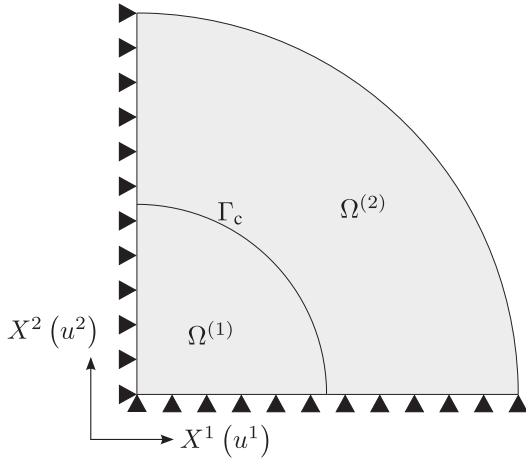
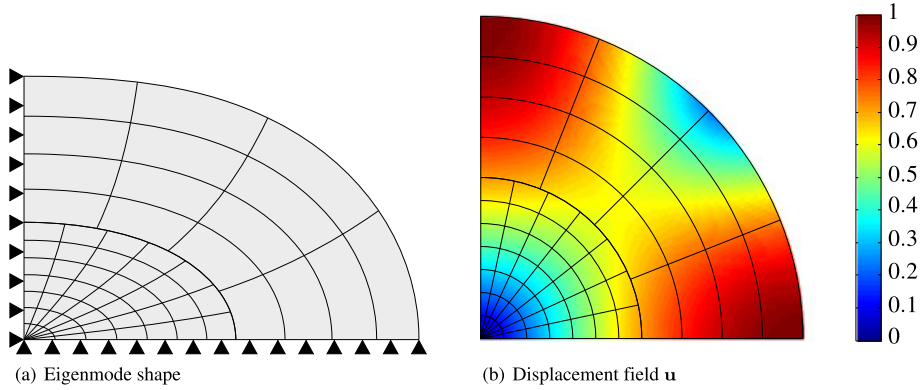
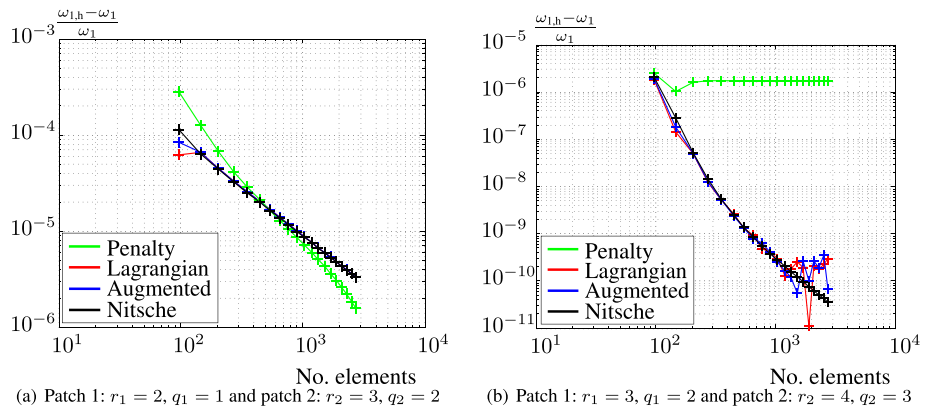


Figure 30. Circular disk: problem placement.

Figure 31. Circular disk: postprocessing. Visualization of the eigenmode shape corresponding to the eigenfrequency $\omega_1 = 1.1822$. Patch 1 has been modeled with 49 elements and polynomial degrees $r_1 = 4, q_1 = 3$, and patch 2 has been modeled with 16 elements and polynomial degrees $r_2 = 6, q_2 = 5$. (a) Eigenmode shape and (b) displacement field \mathbf{u} .Figure 32. Circular disk: convergence of the 1st eigenfrequency in the relative error. (a) Patch 1: $r_1 = 2, q_1 = 1$ and patch 2: $r_2 = 3, q_2 = 2$ and (b) patch 1: $r_1 = 3, q_1 = 2$ and patch 2: $r_2 = 4, q_2 = 3$.

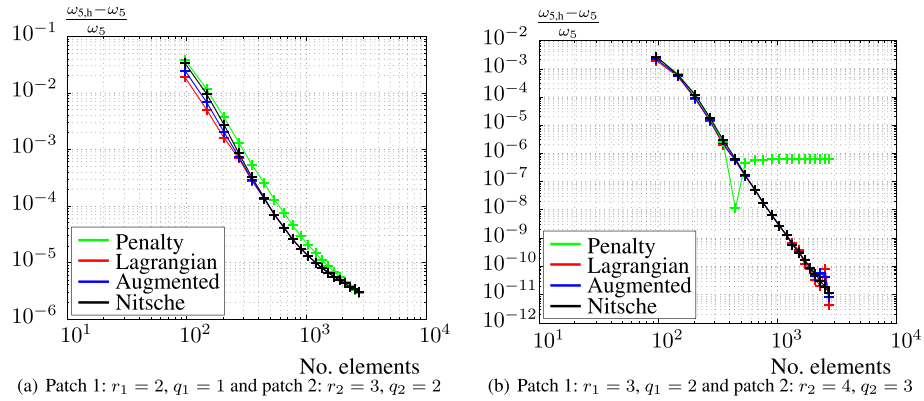


Figure 33. Circular disk: convergence of the 5th eigenfrequency in the relative error. (a) Patch 1: $r_1 = 2$, $q_1 = 1$ and patch 2: $r_2 = 3$, $q_2 = 2$ and (b) patch 1: $r_1 = 3$, $q_1 = 2$ and patch 2: $r_2 = 4$, $q_2 = 3$.

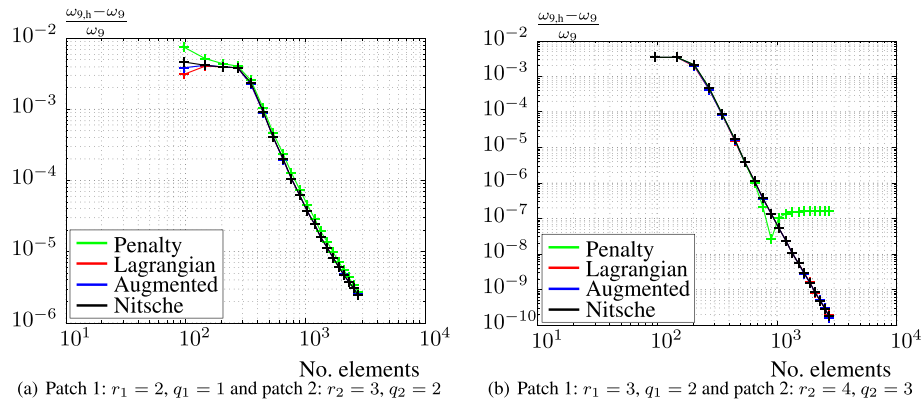


Figure 34. Circular disk: convergence of the 9th eigenfrequency in the relative error. (a) Patch 1: $r_1 = 2$, $q_1 = 1$ and patch 2: $r_2 = 3$, $q_2 = 2$ and (b) patch 1: $r_1 = 3$, $q_1 = 2$ and patch 2: $r_2 = 4$, $q_2 = 3$.

10^{-5} , whereas the rest of the methods are converging towards the solution with the Nitsche being the most stable compared to the Lagrange multiplier ones, see Figure 32(b).

Then, convergence in the eigenfrequency $\omega_5 = 3.2674$ is shown in Figure 33. Evidently, the convergence rates are higher for high polynomial degrees, and the leveling off point for the penalty method is detected in the range of 10^{-6} . Finally, convergence in the eigenfrequency $\omega_9 = 4.1859$ is shown in Figure 34. Here, the leveling off point for the penalty method is detected in the range of 10^{-7} . From the aforementioned texts it can be concluded that the higher eigenfrequencies can be approximated easier than the lower ones especially for high polynomial degrees. The eigenvalue analysis has shown that the DDMs can be easily extended from the steady-state to the transient cases without significant effort. It must be also noted that there are interface coupling modes for the decomposed problems, in contrast to the single domain problems. However, those modes appear to be of high eigenfrequencies, meaning that they are the last and the hardest to be triggered in a dynamical process.

5. CONCLUSIONS AND OUTLOOK

This paper combines standard DDMs, for example, penalty, Lagrange multiplier, and augmented Lagrange multiplier methods, with IGA for the analysis of elasticity BVPs in multiple domains. Additionally, a Nitsche-type formulation is proposed in conjunction with a generalized eigenvalue problem for the estimation of a suitable stabilization parameter. This application of the DDMs is essential because complex geometries do not comprise a single NURBS patch.

As the shown examples illustrate, the penalty method works quite well until the method reaches its level off point caused by the remained error in the constraint due to the fixed penalty parameter. A remedy is to increase the penalty parameter, but this would destroy the conditioning of the system. This renders the method not optimal. An improvement is to employ the Lagrange multiplier or the augmented Lagrange multiplier approach. It has been reported that the accuracy of these methods is improved compared to the penalty one. Because both approaches result in a saddle point formulation, the finite dimensional spaces have to be chosen carefully. This is not a trivial problem, and it has been reported that, in some cases, the discrete equation system is ill-conditioned, resulting into oscillatory results. However, the error is minimized satisfactorily, see Section 4. In general, the augmented Lagrange multiplier approach yields better results than the Lagrange multiplier one. The Nitsche method has proven to be the most stable of all the other DDMs with respect to accuracy, robustness, and positive definiteness of the resulting discrete equation system. To obtain a stabilized formulation, a generalized eigenvalue problem must be solved over the interface DOFs. The overall effort is not increased significantly because the solution of eigenvalue problems is restricted on the interface. Moreover, only vector matrix multiplications are involved within the solution of eigenvalue problems, which is inexpensive in terms of computational effort, see for instance [40]. A stable, uniform convergence to the problem's solution has been observed for all the numerical experiments. Thus, the Nitsche method is found to be the most suitable DDM for decomposed linear elastic problems. Further development of the DDMs in the context of IGA may involve the extension of the Nitsche method to nonlinear problems as well as to 3D steady-state or transient problems. Furthermore, it has been numerically shown that the DDMs perform accurately also in cases where the interface parametrizations of the subdomains get singular. However, this observation demands for further fundamental mathematical research.

ACKNOWLEDGEMENTS

This work has been supported by the Deutsche Forschungsgemeinschaft (DFG). This support is gratefully acknowledged herein. Moreover, the authors would like to acknowledge the funding of the International Graduate School of Science and Engineering (IGSSE) at the Technische Universität München, which is part of the German Excellence Initiative.

REFERENCES

- Hughes T, Cottrell J, Bazilevs Y. Isogeometric analysis: CAD, finite elements, NURBS, exact geometry, and mesh refinement. *Computer Methods in Applied Mechanics and Engineering* 2005; **194**:4135–4195.
- Bazilevs Y, Calo VM, Cottrell JA, Evans JA, Hughes TJR, Lipton S, Scott MA, Sederberg TW. Isogeometric analysis using T-splines. *Computer Methods in Applied Mechanics and Engineering* 2010; **199**:229–263.
- Cirak F, Ortiz M. Fully C^1 -conforming subdivision elements for finite deformation thin-shell analysis. *International Journal for Numerical Methods in Engineering* 2001; **51**:813–833.
- Cirak F, Ortiz M, Schröder P. Subdivision surfaces: a new paradigm for thin shell analysis. *International Journal for Numerical Methods in Engineering* 2000; **47**:2039–2072.
- Nguyen-Thanh N, Kiendl J, Nguyen-Xuan H, Wüchner R, Bletzinger KU, Bazilevs Y, Rabczuk T. Rotation free isogeometric thin shell analysis using PHT-splines. *Computer Methods in Applied Mechanics and Engineering* 2011; **200**:3410–3424.
- Schillinger D, Dedè L, Scott MA, Evans JA, Borden MJ, Rank E, Hughes TJR. An isogeometric design-through-analysis methodology based on adaptive hierarchical refinement of NURBS, immersed boundary methods, and T-spline CAD surfaces. *Computer Methods in Applied Mechanics and Engineering* 2012; **249–252**:116–150.
- Scott MA, Borden MJ, Verhoosel CV, Sederberg TW, Hughes TJR. Isogeometric finite element data structures based on Bézier extraction of T-splines. *International Journal for Numerical Methods in Engineering* 2011; **88**:126–156.
- Schmidt R, Kiendl J, Wüchner R, Bletzinger KU. Realization of an integrated structural design process: analysis-suitable geometric modelling and isogeometric analysis. *Computing and Visualization in Science* 2010; **13**:315–330.
- Schmidt R, Wüchner R, Bletzinger KU. Isogeometric analysis of trimmed nurbs geometries. *Computer Methods in Applied Mechanics and Engineering* 2012; **241–244**:93–111.
- Kiendl J, Bletzinger KU, Linhard J, Wüchner R. Isogeometric shell analysis with Kirchhoff-Love elements. *Computer Methods in Applied Mechanics and Engineering* 2009; **198**:3902–3914.
- Kiendl J, Bazilevs Y, Hsu MC, Wüchner R, Bletzinger KU. The bending strip method for isogeometric analysis of Kirchhoff-Love shell structures comprised of multiple patches. *Computer Methods in Applied Mechanics and Engineering* 2010; **199**:2403–2416.

12. Hesch C, Betsch P. Isogeometric analysis and domain decomposition methods. *Computer Methods in Applied Mechanics and Engineering* 2012; **213-216**:104–112.
13. De Lorenzis L, Wriggers P, Zavarise G. A mortar formulation for 3D large deformation contact using NURBS-based isogeometric analysis and the augmented lagrangian method. *Computational Mechanics* 2011; **49**:1–20.
14. Toselli A, Widlund O. *Domain Decomposition Methods-Algorithms and Theory*. Springer-Verlag Berlin Heidelberg: Berlin Heidelberg, Germany, 2005.
15. Bazilevs Y, Hsu M-C, Scott MA. Isogeometric fluid-structure interaction analysis with emphasis on non-matching discretizations, and with application to wind turbines. *Computer Methods in Applied Mechanics and Engineering* 2012; **249-252**:28–41.
16. Deparis S, Discacciati M, Quarteroni A. A domain decomposition framework for fluid-structure interaction problems. In *Computational Fluid Dynamics 2004*, Groth C, Zingg DW (eds). Springer Berlin Heidelberg, 2006; 41–58, DOI: 10.1007/3-540-31801-1_4.
17. Felippa C, Park K, Ross M. A classification of interface treatments for FSI. In *Fluid Structure Interaction II*, Vol. 73, Bungartz H-J, Mehl M, Schäfer M (eds). Springer Berlin Heidelberg, 2010; 27–51.
18. Hsu MC, Akkerman I, Bazilevs Y. Wind turbine aerodynamics using ALE-VMS: validation and the role of weakly enforced boundary conditions. *Computational Mechanics* 2012; **50**:499–511.
19. Popp A, Gee M, Wall W. Mortar finite element methods for non-matching meshes in contact dynamics, fluid dynamics and FSI. *Abstract at the 84th Annual Meeting of the International Association of Applied Mathematics and Mechanics (GAMM2013)*, Novi Sad, Serbia, 2013; 18–22.
20. Haslinger J, Dostál Z, Kučera R. On a splitting type algorithm for the numerical realization of contact problems with Coulomb friction. *Computer Methods in Applied Mechanics and Engineering* 2001; **191**:2261–2281.
21. Wriggers P. *Computational Contact Mechanics*. Wiley: Chichester, United Kingdom, 2002.
22. Korneev V, Langer U. Domain Decomposition Methods and Preconditioning. *Encyclopedia of Computational Mechanics*, Vol. I. Wiley, 2004.
23. Babuška I. The finite element method with penalty. *Mathematics of Computation* 1973; **27**:221–228.
24. Zienkiewicz O, Taylor R, Zhu J. *The Finite Element Method, Its Basis and Fundamentals*, 6th edn. Elsevier, Oxford: Oxford, United Kingdom, 2005.
25. Unger R, Haupt MC, Horst P. Application of Lagrange multipliers for coupled problems in fluid and structural interactions. *Computers and Structures* 2007; **85**:796–809.
26. Bernardi C, Maday Y, Patera AT. A new nonconforming approach to domain decomposition: the mortar element method, *Technical Report Universit Pierre et Marie Curie*, Paris, France, 1990.
27. Brezzi F. A discourse on the stability conditions for mixed finite element formulations. *Computer Methods in Applied Mechanics and Engineering* 1990; **82**:27–57.
28. Fritz A, Hüeber S, Wohlmuth B. A comparison of mortar and nitsche techniques for linear elasticity. *CALCOLO* 2004; **41**:115–137.
29. Farhat C, Roux F. A method of finite element tearing and interconnecting and its parallel solution algorithm. *International Journal for Numerical Methods in Engineering* 1991; **32**:1205–1227.
30. Kleiss SK, Pechstein C, Jttler B, Tomar S. Ieti isogeometric tearing and interconnecting. *Computer Methods in Applied Mechanics and Engineering* 2012; **247-248**:201–215.
31. Simo JC, Wriggers P, Taylor RL. A perturbed Lagrangian formulation for the finite element solution of contact problems. *Computer Methods in Applied Mechanics and Engineering* 1985; **50**:163–180.
32. Nitsche J. Über ein Variationsprinzip zur Lösung von Dirichlet-Problemen bei Verwendung von Teilräumen, die keinen Randbedingungen unterworfen sind. *Abhandlungen aus dem Mathematischen Seminar der Universität Hamburg* 1971; **36**:9–15.
33. Bazilevs Y, Hughes TJR. Weak imposition of dirichlet boundary conditions in fluid mechanics. *Computers & Fluids* 2007; **36**:12–26.
34. Hsu MC, Akkerman I, Bazilevs Y. Finite element simulation of wind turbine aerodynamics: validation study using nrel phase vi experiment. *Wind Energy* 2013. DOI: 10.1002/we.1599.
35. Hsu MC, Bazilevs Y. Fluid-structure interaction modeling of wind turbines: simulating the full machine. *Computational Mechanics* 2012; **50**:821–833.
36. Akkerman I, Bazilevs Y, Benson DJ, Farthing MW, Kees CE. Free-surface flow and fluid-object interaction modeling with emphasis on ship hydrodynamics. *Journal of Applied Mechanics* 2012; **79**:010905.
37. Akkerman I, Dunaway J, Kvandal J, Spinks J, Bazilevs Y. Toward free-surface modeling of planing vessels: simulation of the fridsma hull using ale-vms. *Computational Mechanics* 2012; **50**:719–727.
38. Hansbo A, Hansbo P. An unfitted finite element method, based on Nitsche's method, for elliptic interface problems. *Computer Methods in Applied Mechanics and Engineering* 2002; **191**:5537–5552.
39. Embar A, Dolbow J, Harari I. Imposing Dirichlet boundary conditions with Nitsche's method and spline-based finite elements. *International Journal for Numerical Methods in Engineering* 2012; **83**(7):877–898.
40. Griebel M, Schweitzer MA. *A Particle-Partition of Unity Method-Part V: Boundary Conditions*. Springer: Berlin Heidelberg, Germany, 2002.
41. Tsamasfyros GI, Theotokoglou EE. *The Finite Element Method I and II*. Symmetria: Zografos of Attica, Greece, 2005.
42. Sanders JD, Dolbow JE, Laursen TA. On methods for stabilizing constraints over enriched interfaces in elasticity. *International Journal for Numerical Methods in Engineering* 2009; **78**:1009–1036.

43. Melenk JM, Babuška I. The partition of unity finite element method: basic theory and applications, 1996.
44. Cottrell JA, Hughes TJR, Bazilevs Y. *Isogeometric Analysis: Toward Integration of CAD and FEA*. Wiley: Chichester, United Kingdom, 2009.
45. Bathe KJ. *Finite Element Procedures*. Prentice Hall: New Jersey, the USA, 1996.
46. Griffel DH. *Applied functional analysis*. Dover Publications Inc.: New York, the USA, 2002.
47. Barber JR. *Elasticity*, Second edn., Kluwer Academic Publishers: Dordrecht, the Netherlands, 2002.
48. Timoshenko S, Goodier J. *Theory of Elasticity*. McGraw-Hill: New York, the USA, 1951.